Title: Macaque Brainnetome Atlas: A Multifaceted Brain Map with Parcellation, Connection, and Histology

Authors: Yuheng Lu[1,2†], Yue Cui[1,3†], Long Cao[4,8†], Luqi Cheng[1,11,13], Zhenwei Dong[1,2], Changshuo Wang[1,3,12], Youtong Liu[1,2], Baogui Zhang[1,3,5], Haiyan Wang[1], Kaixin Li[1,10], Liang Ma[1,2], Weiyang Shi[1,2], Wen Li[1,3], Yawei Ma[1,3,12], Zongchang Du[1,2], Jiaqi Zhang[1,2], Hui Xiong[1], Na Luo[1], Yanyan Liu[1], Xiaoxiao Hou[1], Xinyi Liu[1,2], Hongji Sun[1], Jiaojian Wang[9], George Paxinos[7,8], Zhengyi Yang[1*], Lingzhong Fan[1,2,5*], Tianzi Jiang[1,2,5,13*]

Affiliations:

[1] Brainnetome Center, Institute of Automation, Chinese Academy of Sciences, Beijing 100190, China.

[2] School of Artificial Intelligence, University of Chinese Academy of Sciences, Beijing 100049, China.

[3] University of Chinese Academy of Sciences, Beijing 100049, China.

[4] Henan Key Laboratory of Imaging and Intelligent Processing, PLA Strategic Support Force Information Engineering University, Zhengzhou 450001, China

[5] CAS Center for Excellence in Brain Science and Intelligence Technology, Institute of Automation, Chinese Academy of Sciences, Beijing 100190, China.

[6] State Key Laboratory of Brain and Cognitive Sciences, Beijing MRI Center for Brain Research, Institute of Biophysics, Chinese Academy of Sciences, Beijing 100190, China

[7] Neuroscience Research Australia and The University of New South Wales, Sydney, NSW 2031, Australia

[8] Key Laboratory for NeuroInformation of the Ministry of Education, School of Life Science and Technology, University of Electronic Science and Technology of China, Chengdu 610054, China

[9] State Key Laboratory of Primate Biomedical Research, Institute of Primate Translational Medicine, Kunming University of Science and Technology, Kunming 650500, China

[10] School of Mechanical and Power Engineering, Harbin University of Science and Technology, Harbin 150080, China

[11] School of Life and Environmental Sciences, Guilin University of Electronic Technology, Guilin 541004, China

[12] Sino-Danish College, University of Chinese Academy of Science, Beijing 100049, China.

[13] Research Center for Augmented Intelligence, Zhejiang Lab, Hangzhou 311100, China

Corresponding Authors:

*Professor Tianzi Jiang, Brainnetome Center, Institute of Automation, Chinese Academy of Sciences, Beijing 100190, China. (Email: jiangtz@nlpr.ia.ac.cn)

*Professor Lingzhong Fan, Brainnetome Center, Institute of Automation, Chinese Academy of Sciences, Beijing 100190, China. (Email: lingzhong.fan@nlpr.ia.ac.cn)

*Associate Professor Zhengyi Yang, Brainnetome Center, Institute of Automation, Chinese Academy of Sciences, Beijing 100190, China. (Email: zhengyi.yang@nlpr.ia.ac.cn)

[†] The authors contributed equally

Authors Contributions

T.J. proposed the concept and designed the protocol. Y.L., Y.C., L.C., performed the experiments and analyzed the data. H.S., Y.L., H.X., and X.L. prepared the ex vivo samples, and B.Z. performed the MRI scanning. C.W and Z.Y. developed the website. G.P., L.F., and Y.L. contributed to the nomenclature. T.J., L.F., and Z.Y. led the project and supervised the experiments. All authors contributed to the writing of the manuscript.

Abstract

The rhesus macaque (*Macaca mulatta*) is a crucial experimental animal that shares many genetic, brain organizational, and behavioral characteristics with humans. A macaque brain atlas that identifies anatomically and functionally distinct regions is fundamental to biomedical and evolutionary research. However, even though connectivity information is vital for understanding brain functions, a connectivity-based whole-brain atlas of

the macaque has not previously been made. In this study, we created a new whole-brain map, the Macaque Brainnetome Atlas (MacBNA), based on the anatomical connectivity profiles provided by high angular and spatial resolution ex vivo diffusion MRI data. The new atlas consists of 248 cortical and 56 subcortical regions as well as their structural and functional connections. The parcellation and the diffusion-based tractography were comprehensively evaluated with multi-contrast MRI, invasive neuronal-tracing, and Nissl-stained images collected from a single subject and with open-access datasets from other cohorts. As a demonstrative application, the structural connectivity divergence between macaque and human brains was mapped using the Brainnetome atlases of those two species to uncover the genetic underpinnings of the evolutionary changes in brain structure. The resulting resource includes (1) the thoroughly delineated Macaque Brainnetome Atlas (MacBNA), (2) regional connectivity profiles, (3) the postmortem high resolution macaque diffusion and T2-weighted MRI dataset (Brainnetome-8), and (4) multi-contrast MRI, block-face, and section images collected from a single macaque. MacBNA can serve as a common reference frame for mapping multifaceted features across modalities and spatial scales and for integrative investigation and characterization of brain organization and function. Therefore, it will enrich the collaborative resource platform for nonhuman primates and facilitate translational and comparative neuroscience research.

Keywords: *Macaca mulatta, brain atlas, connectivity-based parcellation, diffusion MRI, resting-state functional connectivity, cytoarchitecture, cross-species comparison*

Abbreviation

IPL	*inferior parietal lobe*
IPL.gr	*inferior parietal lobule, gyral rostral part*
IPL.sr	*inferior parietal lobe, sulcal rostral part*
FPO.ci	*frontal parietal operculum, caudointermediate part*
PM.rd	*premotor cortex, rostrodorsal part*
PM.cd	*premotor cortex, caudodorsal part*
PM.i	*premotor cortex, intermediate part*
PM.cv	*premotor cortex, caudoventral part*
PM.rv	*premotor cortex, rostroventral part*

PM.rm	*premotor cortex, rostromedial part*
PM.cm	*premotor cortex, caudomedial part*
SFG.ri	*superior frontal gyrus, rostrointermediate part*
IFG.cd	*inferior frontal gyrus, caudodorsal part*
IFG.cv	*inferior frontal gyrus, caudoventral part*
OrG	*orbital gyrus*
FP	*frontal pole*
FP.d	*frontal pole, dorsal part*
M1	*primary motor cortex*

Introduction

Rhesus macaques have been widely employed to explore the mechanisms of human cognitive functions and to model human brain disorders due to their high similarity in genetics, physiology, and brain structure[1,2]. International brain projects[3–5] utilize non-human primate research as a core source for elucidating the neural basis of cognition and for promoting translational medicine. A macaque brain atlas that delineates the heterogeneous spatial organizations of the brain can provide a link that can be used to translate findings from rhesus macaques to humans. It can characterize distinct regional profiles, including connectivity, architecture, and topography[6,7], and is fundamental to understanding the function, development, and evolution of the brain[8]. The profiles of different brain regions measured by MRI, tracers, and histology uncover the diverse neurobiological properties on different levels[9–11]. So far, only fragmented studies of macaque atlases on a single level, which can reflect only limited aspects of brain organization and function, have been reported. A new macaque brain atlas with a unifying map of parcellations, connections, and histology across scales and with extensive validation has remained elusive.

Macaque brain cartography has as long a history as that of humans[12], and researchers have created various macaque brain atlases in past decades[13–16]. Previous cyto-, myelo-, and chemoarchitectonic delineations of the macaque brain were primarily developed using neuroanatomical methodologies, and the boundaries of brain structures were determined by microstructural anatomical features[14–19]. Unlike traditional histological methods, animal MRI allows for the intact measurement of the brain. Connectivity-based parcellations have emerged to segregate the brain into distinct regions using diffusion and functional MRI[20,21]. Since anatomical connections

are predictors of functional activations from the primary somatosensory[22,23] to the high-order association cortices[24], identifying the functional diversity of brain regions has been constrained by anatomical connections[25]. Anatomical connectivity-based techniques capture global properties by estimating the physical connections between regions, allowing for a more effective characterization of both the areal- and network-level organizations[7]. To the best of our knowledge, a macaque whole-brain atlas based on anatomical connectivity has, until now, been unavailable.

Comprehensive atlases have successfully delineated brain regions based on anatomical connectivity profiles in other primates, specifically humans and marmosets[26,27]. In rhesus macaques, previous studies using anatomical connectivity to define functional borders mainly focused on particular regions, including the prefrontal cortex[28], inferior parietal lobule[29], accumbens nucleus[30], and other areas[31,32]. As a result of the limited scan tolerance of macaques in vivo, we collected high quality postmortem diffusion MRI (dMRI) data to provide a high spatial and angular resolution, something that would not have been possible in an in vivo study. The greater amount of time available in postmortem studies allows for a more precise characterization of the connectivity profiles between regions[33,34] and, thus, benefits connectivity-based parcellations. Accumulating evidence suggests that integrating anatomical connectivity with multi-modal information such as cytoarchitecture and tracers may be vital for elucidating the specialization of brain regions at multiple levels and scales[10,11,35]. The relationship between connection-based and cytoarchitecture-based parcellations has rarely been explored although some studies have implied that they converge in some brain regions[9,28,36]. MRI, tracer, and Nissl-stained sections of a single monkey, as utilized in this study, could help to link the macroscopic parcellation and connections with microscopic architectures[37].

In the current study, we present a fine-grained anatomical connectivity-based macaque brain atlas, the Macaque Brainnetome Atlas (MacBNA), using high spatial and angular resolution dMRI images of 8 postmortem monkeys acquired with an ultra-high field 9.4T MRI scanner. We also present a set of tracer and Nissl-stained sections from another monkey brain to integrate the MacBNA with meso-scale connections and cytoarchitectonic properties. As an application of the uniquely-constructed Brainnetome macaque and human atlases, we mapped the structural divergency map of those two species based on connectivity and studied how the map relates to transcriptomes. We will release the resource, including the MacBNA and the corresponding

multi-modal connectomes, the postmortem monkey dMRI data, the block-face images, and the section images, for open access.

Results

An overview of the data, mapping, and evaluation of the Macaque Brainnetome Atlas is summarized in Fig. 1. First, diffusion MRI data with high angular and spatial resolutions from eight ex vivo monkeys (Brainnetome-8) (Fig. 1A, left panel) were acquired from a 9.4 T MRI scanner. The advantages of Brainnetome-8 were quantitatively compared with two other macaque datasets, Oxford-I[38] and TVB[39], from open resources. Tracer and Nissl-stained sections from another monkey, R04, (Fig. 1A, right panel) were acquired for the subsequent evaluation of the parcellation and connections. Second, we constructed a fine-grained connectivity-based atlas of the macaque brain, MacBNA, using the Brainnetome-8 (Fig. 1B, left panel). Then, the structural and functional connectomes were identified based on the MacBNA using Brainnetome-8 and Oxford-II[40], respectively (Fig. 1B, middle panel). We mapped the cross-species structural divergence based on connectivity using the Brainnetome atlases for macaques (MacBNA) and humans (HumBNA) and explored the genetic mechanism underlying the evolutionary changes in brain connectivity (Fig. 1B, right panel). Finally, we evaluated the MacBNA in three ways: 1) The cyto-boundary of the R04 Nissl-stained images was compared with the MacBNA at a microstructural level (Fig. 1C, left panel). 2) The diffusion-based structural tractography was validated with neuronal-tracing connectivity (Fig. 1C, middle panel). 3) The distance-controlled boundary coefficient (DCBC) was used to compare the MacBNA with other macaque atlases (Fig. 1C, right panel).

Quality Assessment of Brainnetome-8

High quality dMRI images allow for fine-detailed identification of white matter, leading to accurate estimation of structural connections. Eight ex vivo macaque brains (Brainnetome-8) were soaked with 0.1% gadolinium contrast media for a month to substantially reduce the T1 relaxation time and to improve the quality of the MRI images before scanning with a 9.4 T Bruker MRI scanner. Then, high spatial and angular resolution dMRI data (0.45^3 mm, 180 multi-shell directions) were acquired for a total of more than 1800 hours. Two other public-available macaque datasets, Oxford-I (ex vivo, 0.6^3 mm, 120 single-shell directions) and TVB (in vivo, 1.0^3

141 mm, 64 single-shell directions), were used for comparison with the Brainnetome-8. A gray-matter structure (Fig.
142 2A) that bridges the caudate nucleus and putamen and can be recognized in the Brainnetome-8 was attributed
143 to the high spatial resolution. The primary orientation of the fibers within the bridge in the Brainnetome-8
144 revealed that it connected the two subcortical nuclei, but the fibers were either invisible or unclear in the other
145 two datasets. The high resolution could reduce the partial volume effect (PVE) and help dissect tracts from
146 crossing fibers. A tract that was located lateral to the inferior longitudinal fasciculus (ILF) originated from the
147 caudal part of the ILF and then coursed vertically, emerging to the caudal part of the superior longitudinal
148 fasciculus (SLF)[41,42]. It was visually identified in Brainnetome-8, but it was hard to dissect in either the Oxford-
149 I or the TVB (Fig. 2B). More accurate tractography could be ensured because the Brainnetome-8 had the highest
150 ratio of voxels that contained three fibers (i.e., crossing fibers) and the lowest uncertainty of the orientation
151 estimation using FSL (Figs. 2C, D). A 29×91 tracer connection matrix from an open resource[34,43] was used to
152 elucidate the differences across the three datasets taking the distances between regions into consideration (bin
153 step = 1 mm). The correlation (Pearson's *r*) between the dMRI and the tracer connections showed that the
154 Brainnetome-8 improved the identification of long-range connections although its correlation was similar to
155 that of the Oxford-I for distances less than 20 mm. Also, the ex vivo datasets had substantial advantages over
156 the in vivo one at all distances (Figs. 2E, F).

157 **Structural Connectivity-based Parcellation of Macaque Brains**

158 Using the 8 ex vivo high-quality dMRI dataset, we created a fine-grained whole-brain parcellation of macaque
159 brains based on structural connectivity. Following the protocols used in the HumBNA construction[26], the whole
160 brain was first delineated into 29 initial seed units, each of which was parcellated into multiple subdivisions
161 based on its connectivity with the optimal cluster number determined by three cluster indices (Figs. 3A-F). The
162 whole brain was finally divided into 248 cortical and 56 subcortical subregions with each hemisphere having
163 an equal number of regions (Figs. 4A, B). To evaluate the validity of the MacBNA, DCBC was used to measure
164 the homogeneity and heterogeneity of the parcellations using structural connectivity. DCBC is an unbiased
165 criterion that can compare within-parcel to between-parcel similarity considering the spatial autocorrelation of
166 the brain data and the scale of the parcellations. In other words, a higher DCBC indicates that the parcellation
167 provides a brain topography with higher within-parcel similarity and higher between-parcel dissimilarity. We

compared the DCBC of the MacBNA using the structural connectivity of each vertex/voxel with other existing parcellations of macaques, including Paxinos et al.'s[18], CHARM[19], Saleem et al.'s[44], and Markov et al.'s[43]. The results in Fig. S8 demonstrate that MacBNA achieved the best performance for the delineation of the macaque brain based on structural connectivity (paired *t* test, FDR corrected $P < .0001$). We also examined whether there is bias in the distribution of the parcellation boundary located in the gyri or sulci when using the 'sulc' map generated by Freesurfer[45]. The ratio of the MacBNA boundary vertices that are located in gyral regions (sulc > 0) to those in sulcal regions (sulc < 0) was not significantly greater than random using 10000 permutations ($P_{spin} > .05$) (Fig. S16).

Multifaced Mappings and Evaluation of Premotor Cortex

Taking the premotor cortex (PM) as a representative instance (another example of the OrG in Fig. S4, S5), we identified seven subregions, the PM.rd, PM.cd, PM.i, PM.cv, PM.rv, PM.rm, and PM.cm, based on the local maximal positions of their clustering indices (Fig. 5A, left panel) (Fig. S2A). Using the data from the multiple subjects collected in Brainnetome-8, we calculated the population probabilistic map of each subregion to reveal the individual variation (Fig. 5A, middle panel), which indicates the stability of the parcellation map across subjects. The structural connectivities of the PM.cd and PM.i (Fig. 5A, right panel) show the differences in their connection patterns with the whole brain. Specifically, the PM.cd showed stronger connections with the medial cortex and posterior intraparietal regions, and the PM.i had stronger connections with the ventral premotor and sensorimotor areas.

A gradient analysis using a diffusion map algorithm[46] based on the structural and functional connectivity of this premotor region shows that the first gradients of the two modalities had a high correlation coefficient ($r = 0.98$, $P_{spin} < .001$, Figs. 5B, C). For the second and the third gradients, the correlations decreased to $r = 0.689$ ($P_{spin} < .001$) and $r = 0.205$ ($P_{spin} < .001$), respectively (Figs. S2C, D). A 2D visualization of the gradients using t-SNE[47] for each subregion presented a clustering pattern for both the structural and functional modalities, visualizing our parcellations from the viewpoint of gradients.

To explore the cytoarchitectonic variations between the regions, we collected Nissl-stained sections from a postmortem monkey (ID: R04) and mapped the MacBNA parcellation to the corresponding Nissl slice space (Fig. 5D) with the black boundary delineating the subregions of the MacBNA in the left hemisphere and the

195 white and orange dots marking the respective locations of the PM.cd and PM.i. The density profiles of those
196 two regions (marked as box A in Figs. 5D, E) along the pial and white surfaces was extracted to obtain the
197 cytoarchitecture-based boundary. A sliding window procedure was used to calculate the distance between the
198 neighboring blocks (see **Methods** for details). The distance function of the profile positions located the maximal
199 point as a peak with the block size set at 20. The block size was set from 11 to 24 to ensure that the maxima
200 were robust and independent of this parameter (Fig. S3A). A Hotelling's T^2 test was used to confirm the
201 significance of the peak ($P < .05$), and the two neighboring sections underwent the same procedure to ensure
202 that the peak location was stable and not a false positive caused by artifacts or outliers (Figs. S3B, C). The cyto-
203 boundary based on the profile density analysis (position 81, red line in Fig. 5E left panel) was close to the
204 boundary determined by the connectivity (purple line) (distance between boundary centers = 0.79 mm). Fig. 5E
205 (middle panel) shows the mean density profiles of the PM.cd and PM.i from the pial to the gray/white surface.
206 A permutation test (10000 samples) was utilized to test the significance of the difference in density profiles
207 between the two subregions ($P < .001$, Fig. 7E). A detailed laminar structure of a column of each subregion (Fig.
208 5E right panel) shows that column A, which was selected from the PM.i (as marked with arrows in Fig. 5D),
209 had a denser layer III while column B, which was selected from the PM.cd, had larger pyramidal cells in layer
210 III. The different aspects of the cytoarchitectonic analysis collectively explained our connectivity-based
211 parcellation at a microscopic level.

212 The glial framework allows for an estimation of the orientation of the fibers in the white matter at a high
213 spatial resolution (44 microns in our study) and could be used for tracking tiny tracts like U-fibers that might
214 not be reconstructed directly via MRI due to its insufficiently high resolution. Fig. 5F shows the principal
215 orientation organization that was encoded by the RGB color of the stained section using the glial framework,
216 which delineated the anatomical structures of major tracts such as the corpus callosum (CC) along the left-right
217 axis and the external capsule (EC) along the inferior-superior axis (Fig. 5F). A qualitative comparison of the
218 fitting orientation between the DTI and the glial framework revealed their consistency in some major tracts (Fig.
219 S7). A tiny tract was reconstructed directly via the glial framework that connected the neighboring gyral regions
220 when seeded from the area below the sulci (marked in box B in Fig. 5F). Constructing the glial framework takes
221 advantage of the high resolution of the Nissl sections and is useful as a complement to dMRI.

222 **Comparison of Diffusion-based Tractography and Neuronal-tracing Connectivity**

223 Three injection sites, the IFG.cv, SFG.ri, and IFG.cd, of R04 were coordinated with the MacBNA as the
224 reference system (Fig. 6A). We found that one of those three targets (IFG.cv) had long-range tracer connections
225 with the inferior parietal regions, such as IPL.gr, IPL.sr, and FPO.ci, while the other two did not. A seed ROI
226 was identified as the intersection of a sphere (radius = 3 mm) centered at the coordinates of the injection site
227 with the white/gray surface in the R04 native diffusion space for subsequent probabilistic tracking. The
228 trajectory of the tractography indicates that more streamlines from the IFG.cv terminated around the IPL regions,
229 consistent with the tracer data (Fig. 6B). The contrast between the normalized connection strength of the regions
230 identified by the R04 dMRI, as well as that of the connections from the Brainnetome-8, was similar to that of
231 the number of tracer-labeled neurons (Fig. 6C).

232 To reveal the level of agreement between the structural connections and those derived from tracer data
233 more comprehensively, an approximate comparison was made based on the forementioned open-access tracer
234 data, which contains more connections across the whole macaque brain. The injection sites and tracer matrix
235 were mapped to our atlas since the original targets were identified in Markov et al.'s atlas[43], which has 91 areas.
236 The structural connection based on tractography with the Brainnetome-8 dMRI data was fractionally scaled and
237 log-normalized as in Markov et al.'s study. The connection matrix of the 20 selected regions indicates that the
238 dMRI and tracer data had similar patterns (Fig. 6D), as indicated by a high Pearson's correlation coefficient of
239 $r = 0.71$, $P < 10^{-6}$ (Fig. 6E). The correlation decreased to 0.5 when the areal distance was greater than 20 mm,
240 while the area-under-curve scores between the binarized connections matrices were always above 0.7 when the
241 areal distances ranged from 0 to 40 mm (Fig. 6E). These findings reveal that dMRI was better at identifying
242 short-range connections than long-range connections and had a good sensitivity and specificity regarding
243 whether a connection was present or absent between regions for not only short- but also long-range connections.

244 **Cross-species Structural Connectivity Divergence Based on the Macaque and Human Brainnetome**
245 **Atlases**

246 The well-delineated parcellations based on MacBNA and HumBNA, which were both based on connectivity,
247 provided a basis for exploring the evolutionary structural connectivity divergence between macaque and human

248 brains. The regional structural connectivities of those two species were represented as the connection probability
249 based on 42 homologous major tracts, i.e., connectivity blueprint[48] (Fig. 7A). We denoted the structural
250 divergence as the symmetric Kullback-Leibler (KL) distance between the group-wise connectivity blueprints of
251 each region from the MacBNA and each region from the HumBNA. The divergence map represents the
252 minimum divergence of each region of the HumBNA from each region of the MacBNA, indicating that the
253 dorsal prefrontal, posterior parietal, and medial prefrontal cortices had greater divergence, while the visual and
254 temporal cortex had less divergence (Fig. 7B). The divergence map was also significantly correlated with some
255 existing brain maps such as the developmental expansion, cerebral blood flow, and glucose metabolism maps
256 (Fig. 7C) from neuromaps[49]. Furthermore, partial least squares regression (PLSR) was used to investigate the
257 association between the divergence map and the gene expressions using the Allen Human Brain Atlas (AHBH)
258 transcriptome dataset[50]. The first component of the PLSR (PLS1 score, explained variance = 20.4%, $P_{spin} < .05$)
259 had the highest Pearson's correlation with a divergence map of $r = 0.47$ ($P_{spin} < .05$) (Fig. 7D). The 2257 genes
260 with the most positive and negative weights ($|Z| > 3$) were enriched in the intelligence, cognition, and mental
261 disease-related gene sets, which had been obtained from DisGeNet[51] (Fig. 7F). Finally, these 2257 genes were
262 found to be more significantly overlapped (78 genes) with the human-accelerated genes (391 HAR genes
263 remaining in the 15633 AHBH genes set)[52] using Fisher's exact test ($P < .0001$) (Fig. 7G).

264 Discussion

265 We produced a 152-area (124 cortical and 28 subcortical areas) per hemisphere macaque brain atlas, MacBNA,
266 based on structural connectivity derived from high-quality ex vivo dMRI data and determined connectivity
267 profiles for each subregion. Conjunct analyses with multi-contrast MRI, neuronal tracing, and cytoarchitectonic
268 data from a single macaque collected in the present study and other independent datasets provided
269 comprehensive and enhanced validations for the brain parcellation and connections. Comparative analyses
270 based on the uniformly well-delineated Brainnetome atlases for macaques (MacBNA) and humans (HumBNA)
271 unveiled the evolutionary hierarchical adaptations in structural connectivity and its genetic underpinnings. In
272 addition, the new MacBNA atlas provides a common coordinate framework for spatially integrating large
273 amounts of data across modalities and scales, providing multifaced maps at various levels including

macroscopic brain morphology, structural and functional connectivity, mesoscopic tracer-based connectivity, anatomical microstructures, etc. Therefore, MacBNA, together with the comprehensive data, can be a valuable resource for joint investigations of brain organization and function, which can promote progress in comparative neuroscience and translational medicine.

Brain topography can be characterized from multiple facets including connectivity, cytoarchitecture, and function. Anatomical connectivity is one of the domains that can be used to identify brain spatial heterogeneity, and our atlas preserves the brain topography from the perspective of anatomical connectivity substantially better than other macaque brain parcellations (Fig. S8). Non-human primate studies revealed that cytoarchitecture is partially determined by cortical connectivity[53,54] and that the boundaries identified by the anatomical connections between brain areas conform to some degree to the histological subdivisions of the cortex[8,30,36]. The subdivisions of the IPL gyral area, as well as those of the dorsal and medial areas of the premotor cortex, in the MacBNA are consistent with existing cyto- or myeloarchitectonic atlases[18,55,56]. Compared with histological architecture, which characterizes local properties of cell morphology and laminar structure, anatomical connectivity subdivides brain regions by taking advantage of the extensive interconnections within the whole-brain that govern the nature and flow of neural activity, reflecting the underlying functional topography of the brain. For example, we segregated the somatosensory cortex into four subregions that appear to represent the face, forelimb, trunk, and hindlimb fields found in a functional somatotopy study[57] rather than following the cytoarchitectonic parcellations along the rostral-caudal axis (areas 3a, 3b, 1, 2). Area M1 is traditionally considered to be homogeneous within the regions indicated by traditional histological studies[12,14], but our parcellation results for the M1 show a pattern along the ventral-dorsal axis, which closely mirrors the somatotopic organization of this area[58,59], suggesting that the functional specialization of regions underlies the connectivity[60].

Since it is widely accepted that there is no golden standard for parcellating the brain, delineating the brain on multiple scales[7,61] is essential if we are to explore the brain organization comprehensively. Hence, we provided the MacBNA as a reference system to link the macroscopic connectivity with the microscopic neuroanatomy. By using multi-modal and multi-scale data, various profiles for each region, i.e., the structural and functional connectivity, gradients, and cytoarchitecture, could be mapped (Figs. 5). The connection profiles of each subregion enable the functional role of regions to be tentatively inferred and understood[62]. The

heterogeneous connectivity of the regions lying in the peri-arcuate area (Figs. 6B, C) could unveil the functional specificity of those regions. The IFG.cv, which is located in the transition zone between the agranular premotor area 6 and granular area 8, may play a role in controlling the oculomotor as it has a strong connection with the anterior inferior parietal cortex[63], whereas the granular regions SFG.ri and IFG.cd have only no or weak connection. These latter two regions, the SFG.ri and IFG.cd, which lie anterior to the frontal eye field, may be more related to the top-down control of visual attention[64]. The cytoarchitectonic differentiation between regions could be quantified using the histological data[10], giving rise to an observer-independent cytoarchitectonic subdivision (Fig. 5E) that could be compared with other parcellations. Observer-independent cytoarchitectonic analysis avoids the traditional visual inspection of stained sections, and researchers could take advantage of the high-resolution histological images to identify finer-grained subdivisions[55,65]. Since gradient is a popular way to represent brain regions as continuous maps rather than as hard-edged parcellations[66–68], it can provide an alternative perspective that can help to reflect the neuroanatomy and explain the parcellation pattern in the gradient space (Figs. 5B, C). A recent study indicated that the dorsal premotor cortex has a cognitive-motor behavioral gradient[69] along the rostral-caudal axis in humans that is consistent with the third structural gradient we found in the PM (Fig. S2). Kahnt et al. proposed that the medial-lateral and posterior–anterior distinctions of the orbitofrontal cortex reflect abstract reinforcers[70], which is similar to the first and third structural gradient of the OrG that we found (Figs. S4, 5). All of these profiles of the brain are complementary to each other and contribute jointly to the formation of brain function. Focusing solely on one will result in a one-sided view of understanding the structure-function tethering of the brain.

Conducting cross-species comparison in a common space[71] is commonly done, but it is also crucial to compare the brain organization with parcellations based on unique architecture. The MacBNA and HumBNA, which were uniformly delineated using structural connectivity, provide an alternative to the traditional cytoarchitecture atlases of macaques and humans for uncovering evolutionary changes. The identified divergence map formed using MacBNA and HumBNA revealed that the greatest evolutionary variation in connectivity between humans and macaques is located in the prefrontal and parietal cortices, which are closely related to high-level cognitive functions[72,73] and are supported by a higher metabolism rate[74]. However, the fact that the relatively new brain organization of human from an evolutionary timescale perspective may make itself more vulnerable to stress, trauma, or neurodevelopmental conditions, resulting in the psychiatric disorders[75,76]

330 that we found genetic evidence for using the AHBH transcriptomes datasets (Fig. 7F). The association between
331 the divergence map and gene expression revealed in this study adds to our understanding of how transcriptional
332 specialization shaped the brain structure, leading to not only higher cognition and intelligence but also to mental-
333 related diseases[77,78]. The accumulation of postmortem dMRI data from primates makes it possible to generalize
334 the parcellation framework to construct connectivity-based atlases[79], facilitating a polygenetic comparison
335 across primates.

336 The datasets in this study include not only a new macaque atlas but also its corresponding structural and
337 functional connectomes, as well as high-quality dMRI and tracer data and Nissl-stained sections, making
338 MacBNA a multi-scale multi-modal atlas resource. One of the challenges associated with dMRI is its inability
339 to produce images with high resolution. This low resolution limits the dissection of the white matter bundles
340 and the mapping of the tract pathways in living humans or other primates. However, ex vivo dMRI has the
341 advantage of higher field strength and longer scan duration with tailored pulse sequences[80] and contrast agents
342 to improve the data quality[27]. Compared with the other two public datasets, Brainnetome-8 could be used to
343 depict the detailed neuroanatomy of not only the major tracts but also tiny/thin tracts because of its relatively
344 high spatial resolution[81–83]. Using Brainnetome-8 enabled us to resolve more crossing fibers within the white
345 matter and sharpen the probabilistic estimation of the fiber orientation (Fig. 2) since using multiple angular
346 contrast and a multi-shell acquisition strategy with high b-values as we did can provide better estimates of
347 different diffusion compartments and lower the uncertainty of the probabilistic fitting of the diffusion
348 orientation[84,85]. The connections obtained using tracers, tractography, and the glial framework[8–10] allow for
349 cross-validation by independent aspects of brain properties. Brainnetome-8 performed better than the other
350 released datasets of the ex vivo macaque brain when identifying long-range connections. This is consistent with
351 findings that a higher spatial and angular resolution is important for improving the level of agreement between
352 tracers and dMRI[33]. A recently developed technique[37] utilized the local organization of glia cells from Nissl-
353 stained sections to reconstruct the fiber orientations at a microscale resolution. A qualitative comparison
354 revealed its good correspondence with the dMRI across species[37,86], as we found in a single macaque animal
355 (Fig. S7). The extremely high in-plane spatial resolution provided by the glia framework also allowed for the
356 reconstruction of tiny U-fibers (Figs. 5F, S4F), compensating for the lack of resolution in dMRI.

In summary, we present a new macaque brain atlas, the MacBNA, based on structural connectivity with high spatial and angular resolution dMRI images. The MacBNA consists of not only a plausible and fine-grained parcellation but also the detailed macroscopic connections of each subdivision. It can provide a reliable reference system for coordinating and integrating a variety of types of brain maps, including imaging (e.g., multi-contrast MRI, tracing and Nissl-stained data) and genomics (e.g., transcriptomes and proteomes) data to develop a multifaceted brain map of macaque. The multi-modal multi-scale dataset in this study will also provide an open-access platform for addressing computational issues such as modeling a virtual brain and cross-scale image registration. We are still in the process of collecting data to further enrich the MacBNA with additional tracer and staining images. In addition, the conceptual framework underlying the construction of the Brainnetome Atlas can be extended to other species for comparative research. Thus, we envision that the Macaque Brainnetome Atlas and the associated dynamic multi-modal multi-scale resources will play a role in cross-species comparisons, translational medicine, and computational modeling.

Methods

Animals and Data Acquisition

Eight post-mortem monkeys (Brainnetome-8) were utilized to delineate the atlas and construct the structural connectomes, and another two open access cohorts of 6 ex vivo animals (Oxford-I) and 8 in vivo animals (TVB) were used for validation. Another open access in vivo dataset (Oxford-II) was used to map the resting-state functional connectomes. An additional female adult macaque was scanned to acquire multi-contrast MRI, neuronal tracing, and Nissl-stained histological images covering the whole-brain. All animal procedures in this study were approved by the Ethics Committee of the Biomedical Research of Institute of Automation, Chinese Academy of Sciences (No. IA-202032).

MRI of Brainnetome-8 and Open-access Datasets

The Brainnetome-8 consisted of 2 male and 6 female (age = 5.6±1.06 years old) adult monkeys (*Macaca mulatta*). Each monkey was intraperitoneally injected with an overdose of pentobarbital. After a careful confirmation of deep anesthesia, a transcardial perfusion was performed with 500 ml of phosphate-buffered saline (PBS) solution containing 1% heparin (pH 7.4) and 0.1% gadolinium-diethylenetriamine pentaacetic acid

383 (Gd-DTPA). After this 500 ml perfusion, the body organs such as the heart and bladder were removed, and the
384 perfusion rate was decreased to 30 ml/min. This was followed by perfusing with a PBS solution containing 4%
385 paraformaldehyde and 0.1% Gd-DTPA. After two hours of perfusion, the head was removed from the body,
386 and the skull was carefully stripped to expose the whole brain. The formalin-fixed macaque brain was soaked
387 in 0.1% Gd-DTPA and 0.1% sodium azide under sterile conditions for 4 weeks to reduce the T1 relaxation time.
388 Prior to imaging, the specimens were transferred to an MRI compatible holder bundled with medical gauze and
389 immersed in Fomblin (Solvay, Brussels, Belgium) to prevent dehydration and susceptibility artifacts; air bubbles
390 on the brain surface were removed with an aspirator.

391 Ex vivo MRI data were acquired on an ultra-high field 9.4T horizontal animal scanner (Bruker Biospec
392 94/30 USR, Ettlingen, Baden-Württemberg). The gradients were equipped with a slew rate of 4570 mT/m/ms
393 and maximum strength 660 mT/m, and the radiofrequency (RF) transmission and reception were achieved with
394 a 72 mm inner-diameter quadrature RF coil. The T2w image for each specimen was acquired with a 3D Turbo
395 RARE sequence: TE = 36 ms, TR = 2000 ms, NEX = 6, matrix size = 240×180×267, resolution = 0.3×0.3×0.3
396 mm, FOV = 72.0×54.0×80.1 mm. The multi-shell dMRI was acquired with a 3D multi-segment echo planar
397 imaging diffusion weighted sequence: TE = 23 ms, TR = 200 ms, bandwidth = 178.5 kHz, NEX = 7, matrix size
398 = 148×120×160, resolution = 0.45×0.45×0.45 mm, FOV = 66.6×54.0×72.0 mm. For 7 of the 8 monkeys, a total
399 of 186 diffusion-weighted images (DWI) with 2 shells were collected, including 6 non-diffusion images for b =
400 0 s/mm^2, 60 directions for b = 2400 s/mm^2 and 120 directions for b = 4800 s/mm^2, with a total scan duration of
401 about 243 hours. The scanning for the last monkey consisted of 6 b = 0 s/mm^2, 30 b = 2400 s/mm^2, and 90 b =
402 4800 s/mm^2 DWI data and lasted about 145 hours.

403 The Oxford-I and Oxford-II datasets were both from an open resource, PRIME-DE[3,38,40]. The Oxford-I
404 dataset included 4 male and 2 female ex vivo subjects. Briefly, it consisted of 16 non-diffusion and 128 b =
405 4000 s/mm^2 volumes with 0.6 mm isotropic resolution. The Oxford-II dataset consisted of 20 male in vivo
406 macaque monkeys with 0.5 mm isotropic T1w and 2 mm isotropic resting-state images (TR = 2 s, 1600 volumes).
407 The in vivo TVB dataset was obtained from another public resource[39] that included 8 male macaque monkeys
408 and consisted of 0.5 mm isotropic T1w images and 1.0 mm isotropic DWI data with 64 directions, b = 1000
409 s/mm^2.

410 ***MRI, Tracer Injection, and Histology of R04***

411 Prior to the surgery, the macaque brain (ID: R04, female, 11 years old, 6.75 kg) was scanned on a 3.0T Simens
412 Prisma scanner to acquire in vivo T1w and T2w images. The T1w images were acquired with a magnetization
413 prepared rapid gradient-echo (MPRAGE) pulse sequence: TE = 2.8 ms, TR = 2.2 s, matrix size = 240×300×320,
414 resolution = 0.5×0.5×0.5 mm, FOV = 120.0×150.0×160.0 mm, and the T2w images were acquired with a single
415 slab three-dimensional turbo spin echo (SPACE) sequence: TE = 0.39 s, TR = 3.2 s, matrix size = 240×300×320,
416 resolution = 0.5×0.5×0.5 mm, FOV = 120.0×150.0×160.0 mm. After the establishment of anesthesia, the scalp
417 was incised under the guidance of a coordinate navigation system (Brainsight Vet, Rogue Research, United
418 States) for the subsequent tracer injection. Three retrograde tracers (1% CTB488, CTB555, CTB647, Invitrogen,
419 United States) were injected with the site coordinates pre-determined in structural MRI images under the path
420 planning of the navigation system. Injections were carried out separately through glass pipettes attached to
421 pumps (Nanoliter 2010 Injector, World Precision Instruments, United States) and a controller (Mico4 Micro
422 syringe Pump Controller, World Precision Instruments, United States) with a volume of 500 nl. 15 days after
423 the surgery, the animal was sacrificed and the brain was extracted and fixed following the protocol mentioned
424 above. The brain was then scanned on a 9.4T scanner to acquire a whole-brain dMRI dataset with the same
425 acquisition parameters as the Brainnetome-8 dataset except that the isotropic resolution was 0.6 mm^3 with 4
426 diffusion gradient directions b = 0 s/mm^2 and 60 b = 4800 s/mm^2. After the cerebellum was removed from the
427 brain tissue, sucrose protection was utilized, and the tissue was frozen with dry ice and embedded in optimal
428 cutting temperature compound (OCT) before sectioning. Coronal sections with a thickness of 40 μm were
429 obtained using a cryotome (Cryostar NX70, Thermo Fisher, United States) and block-face images were acquired
430 for all sections, using a camera. One in every 12 consecutive sections was selected for Nissl staining to visualize
431 the cell bodies, following the standard procedure. One in every 6 sections was used for fluorescence imaging.
432 Each selected section was imaged with the microscopy (Axio Scan. Z1, Zeiss, Germany) at 0.22 μm in-plane
433 resolution. For those sections with severe artifacts, whenever possible the neighboring sections were chosen for
434 imaging as alternatives.

435 **Preprocessing**

436 For the ex vivo subjects, the T2w or b0 images were contrast inverted[33] as a fake T1w to reconstruct the surfaces
437 via the HCP-NHP pipelines[87]; for the in vivo subjects, the surfaces were reconstructed using the T1w structural

438 images directly. Then those surface data were all resampled to 10k and 32k for the subsequent analysis.
439 Additionally, the high-contrast b0 image of a post-mortem template named CIVM[88] was utilized to reconstruct
440 the CIVM surface for the subsequent definition of seed regions (Fig. 3A).

441 Preprocessing of the diffusion MRI data was performed in the same way across all the subjects. Specifically,
442 eddy current correction, unringing, and denoising were performed using FSL[89] and MRtrix3[90]. Finally, fiber
443 orientation distributions (maximal number of fibers per voxel = 3) were estimated using Bedpostx in FSL. The
444 uncertainty provided by Bedpostx characterized the width of the distribution for each orientation. Specially, the
445 averaged b0 images underwent intensity bias correction using N4BiasCorrect[91] for registration to the CIVM
446 template.

447 A recently available fMRI pipeline[19] was adapted to preprocess the resting-state fMRI data following the
448 preprocessing process in published studies[92,93]. Briefly, it included despiking, motion correction, global scaling,
449 and nuisance regression of the white matter (WM) and cerebrospinal fluid (CSF) signals, bandpass filtering
450 (0.01–0.1 Hz), and co-registration to native anatomical space. Then the denoised resting-state fMRI data was
451 projected to the CIVM midthickness surface and smoothed with FHWM = 3 mm.

452 The restacked 3D block-face image was used as an intermediate for the coregistration between the dMRI
453 and section images. The Macaque Brainnetome Atlas was first non-linearly mapped to the R04 MRI space and
454 then linearly aligned to block-face space using the ANTs algorithm. A coarse linear alignment between the
455 corresponding section and the block-face image roughly located the brain regions of the MacBNA, and the
456 parcellations were then manually inspected and corrected.

457 **Connectivity-based Parcellation**

458 ***Initial Seed Region Definition***

459 Following the protocols that we used in constructing the Human Brainnetome Atlas[26], we identified the initial
460 parcellation units of the macaque brain using previous macaque atlases[16,18,88,94] or delineations of the macaque
461 brain[95]. Splitting the cortical regions was based on landmarks, such as large sulci and gyri, accompanied by
462 some cytoarchitecturally defined boundaries as a complement (Supplement Fig. S1, Tab. S1). The initial seed
463 regions of the subcortex were solely determined by referring to Paxinos et al.'s[18] rhesus monkey brain atlas.

All the regions were delineated in the CIVM template, and then the cortical ones were projected to the CIVM mid-surface to obtain a surface-based segmentation of 21 regions (Fig. 3A).

Surface-based Probabilistic Tractography and Connectivity-Based Parcellation

With 21 cortical seed regions delineated on the surface, a surface-based probabilistic tractography was performed using probtrackx2 in FSL. Taking an initial region as a seed mask (Fig. 3B), 10000 streamlines originating from each vertex were sampled, with a 0.2 curvature constraint, 3200 steps per sample, and a 0.5 mm step length to estimate the vertex-wise connectivity profile. The whole-brain connectivity was smoothed with the tracking target mask resampled to 2 mm to reduce the noise (Fig. 3C). A similarity matrix between each seed vertex was derived from the connectivity matrix and then group-wise averaged. Spectral clustering was used to define the distinct subregions (Fig. 3D) as in our previous study of the human brain[26]. Subcortical regions were parcellated in a similar way, but using tracking in volume space.

Strategies for Choosing Optimal Cluster Number and Hierarchical Parcellation

To obtain a reliable parcellation of each region, we selected the local maxima as the optimal cluster number using a weighted score obtained by aggregating three characteristic cluster indices, Cramér's V (CV), topological distance (Tpd), and hierarchy index (Hi). To validate the robustness of the optimal cluster number, a leave-one-out strategy was used to replicate the identification of local maxima with one subject excluded each time, and we then counted the frequency of each cluster number as a local maximum. These cluster indices were described in detail in Li et al.'s study[96]. An entropy-based aggregate method[97] was utilized to combine a pairwise CV between individuals, a group-level Tpd between hemispheres, and a group-level Hi of each hemisphere into one. The aggregate score of a cluster number *i* was computed according to:

$$score_i = \sum_j h_j \cdot M_{ij} \quad \begin{pmatrix} j = 1,2, \dots m \\ i = 2 \dots K \end{pmatrix} \tag{1}$$

where Mij is the value of cluster i of the jth index, and h_j is the weight of the jth index. Here, m is equal to 3 because CV, Tpd, and Hi were all three used, and K is the maximal cluster number. The weight h_j was computed as:

$$e_j = -\sum_{i=2}^{K} p_{ij} ln p_{ij} \tag{2}$$

$$h_j = \frac{1 - e_j}{\sum_{k=1}^{m}(1 - e_k)} \quad (3)$$

where p_{ij} *is* the normalized M_{ij} to ensure $\sum_{i=2}^{K} p_{ij} = 1$.

A hierarchical parcellation strategy was employed on three initial ROIs (i.e., IPL, STG, and CG). For example, the IPL was parcellated into a sulcal part with four subregions and a gyral part with only one subregion (Fig. 3F), to which the strategy of parcellation was applied again to obtain a finer pattern.

Mapping to Volume and NMT Template

Because the parcellation of the cortex was defined on the brain surface, mapping to the volume space was needed to provide a more general application. Based on the characteristic of columnar anisotropy in the neocortex[27], each voxel was assigned to the label of its closest vertex along the direction perpendicular to the cortical surface. A manual correction and smoothing operation were applied to fix some errors, such as discontinuities or outliers of the parcellation. Since the new atlas was constructed on an ex vivo CIVM template, we also mapped it to the well-known NMT in vivo template[98] using a nonlinear registration provided by ANTs[99] so that our atlas could be used in either setting.

Structural/Functional Connections and Gradients

For each voxel within a brain region of the MacBNA, a probabilistic tractography using 10000 samples was performed as mentioned above to obtain its structural connectivity to the whole brain. Then, we obtained the structural connectivity of a region with the whole brain by averaging the structural connectivity across all the voxels within it. A group-wise structural connectivity map was calculated by normalizing the connectivity of each subject to standard space and then averaging across all the subjects. For the structural connectome, we counted the connected streamlines as the weight of the edge between regions of the MacBNA for each subject. Then, the connectome was normalized and averaged across the subjects.

The functional connectivity of each region with the whole brain was measured by the Pearson's correlation coefficient (Fisher's z-transformed) between its averaged preprocessed time series and that of each voxel of the whole brain. The average group-wise functional connectivity across subjects was tested for statistical significance with a one-sample *t* test (FDR corrected at $P < .01$). For the functional connectome, the parcel-wise Pearson's correlation was calculated as the functional connection between regions and was then Fisher's *z*-

515 transformed. A one-sample *t* test was used to determine the statistical significance on the group level (FDR
516 corrected at $P < .01$).

517 Diffusion map[46] was used on the structural and functional connectivity to obtain gradients at the vertex-
518 wise level. The gradients of the seed region were derived from the similarity matrix between the connectivity
519 of each voxel within the brain region to explore the pattern of changes along specific directions as a complement
520 to and explanation of the parcellation. We selected the top 20 components in the embedding algorithm and
521 visualized the gradients with t-SNE[47] in a 2D dimension.

522 **Evaluation with Tracer Data**

523 Tracer-derived connections are the standard for validating connections identified by diffusion MRI. We
524 evaluated the MacBNA parcellation and the dMRI connections using the collected tracer data from R04 and an
525 open-access tracer resource[43,34].

526 First, we compared the retrograde tracers of the three injected brain regions from the MacBNA with the
527 corresponding connections derived from the dMRI data from the same animal (R04). The seed ROIs were
528 identified as the intersection of a sphere (radius = 3 mm) centered at the coordinates of each injection site and
529 the white/gray surface. 10000 probabilistic streamlines were sampled from each voxel within each seed ROI to
530 estimate the structural connections, as mentioned above, using the dMRI data from R04. The group-wise
531 structural connections of the Brainnetome-8 were also compared with the tracer data from R04.

532 Furthermore, an open tracer resource of macaque data[43,34] was used to evaluate the quality of the
533 Brainnetome-8 dMRI data and to validate the structural connectome derived from MacBNA. The original 29×91
534 tracer connections and the parcellation with 91 cortical regions were used to calculate the correlation with the
535 structural connections using the Brainnetome-8, Oxford-I, and TVB, taking distances between regions into
536 consideration. The distances between the regions of the parcellation from Markov et al.[43] were released in a
537 previous study[100], which identified the minimum white matter trajectories. Furthermore, we mapped the
538 injection sites to the CIVM template surface to determine the target regions in our atlas. Nine target regions
539 from Markov et al.[43] were excluded because the related injection sites did not satisfy a one-to-one mapping, i.e.,
540 multiple sites projected to the same region of our atlas or were located near the boundary. The tracer connectome
541 was mapped to our atlas simply based on the overlap ratio with Markov et al.'s[43] parcellation. This was possible

because Donahue et al.[34] provided the tracer coordinates that Markov et al.[43] had used in their study, enabling us to validate our atlas with Markov et al.'s tracer data. Thus, we obtained a 20×124 transformed tracer-derived connection matrix to compare with the structural connections from MacBNA while considering the areal distances (Fig. S15). Finally, a 20×20 subgraph that represented the connections between the injected regions was extracted from the adapted tracer matrix to calculate the correlation with the dMRI ones. The distances between the regions of MacBNA were determined as the mean distance of the streamlines using dMRI tractography. The dMRI connection matrix was averaged across hemispheres and fractionally scaled and log-normalized for consistency with the tracer connections[34]. Both the tracer and dMRI connection matrices were symmetrized before the correlation to keep them comparable with each other. The connection matrices were also binarized for the calculation of the area-under-curve score to evaluate the sensitivity and specificity of the dMRI connections.

Comparisons with Existing Parcellations

Five digital parcellations based on cytoarchitecture were used to compare with MacBNA. The alternative parcellations include: (1) Paxinos et al.'s brain atlas of macaques, which has a digital 3D version[88] (PTH09); (2) The fifth-level (CHARM_5) and (3) the sixth-level parcellation (CARHM_6) of a hierarchical atlas[19]; (4) Saleem et al.'s digital atlas based on five different histological stains[44] (Saleem); (5) The parcellation that was used in Markov et al.'s study[43] to navigate the injection sites of tracer for which we used its digital version[34] (Markov).

We compared the six parcellations using a homogeneous metric, DCBC. The basic idea underlying DCBC[101] is that any two vertices/voxels within the same region should have more similarity between their structural connectivity profiles than those belonging to distinct regions. Taking the spatial smoothness of brain data into consideration, DCBC binned each vertex/voxel pair (bin step = 1 mm) based on their geometric distance ranging from 0 to 100 mm and then compared the similarity between the within- and between-parcel within each bin. A higher DCBC indicates that the parcellation reflected a more homogeneous topography based on structural connectivity. The DCBC of MacBNA was compared with that of the other parcellations across subjects using paired *t* tests and was then FDR corrected to test the statistical significance.

Cytoarchitectonic Analysis

Cytoarchitectonic Boundary

The digitized images of the Nissl-stained sections were used for the cytoarchitectonic analysis as Amunts et al.[10] did. Briefly, the images were down-sampled to 22 μm and smoothed to reduce noise and artifacts. The optical density profiles of the regions of interest, which captured the laminar changes, were extracted orthogonally to the surface. The features vectors extracted from the profiles were used to measure the Mahalanobis distance between neighboring blocks. A sliding window procedure (11 <= block size <= 24) determined the peak (maxima) of the distance function. A Hotelling's T^2 test was used to confirm the statistical significance of the peak. The peak locations identified using multiple block sizes were also evaluated by comparing them with maxima locations at neighboring stained sections to exclude the false positive peaks caused by artifacts or outliers (Figs. S3, S6).

Glial Framework

The glial framework was obtained by orientation estimation and fiber tractography using Schurr and Mezer's[37] method. In short, a structure tensor analysis was used to fit the local fiber orientations according to the spatial distribution of the glial cells. The tile size was set at 44 microns (i.e., 200 pixels) with $\rho = 15$ and $\sigma = 3$ as the default. A white matter mask was generated using a semi-automatic annotation tool[102] based on the contrast between the gray and white matter in each Nissl slice. The principal direction estimated using dtifit in FSL with dMRI data from the same monkey was aligned to block-face space for comparison with the orientation obtained from the glial organization. The white matter pathway was reconstructed using fiber assigned by continuous tracking (FACT)[103], a deterministic tractography algorithm in MRtirx3[90]. Step size was set at 3 voxels and the maximal angle was 60°. The seed mask was located in the white matter and 25 streamlines were seeded for each voxel.

Cross-species Structural Divergence Based on Brainnetome Atlases and Its Association with Transcriptome

42 homologous tracts (38 association and 4 commissure) were carefully dissected automatically with XTRACT[104] to characterize the connectivity blueprint[48,104] of each region for each macaque in the Brainnetome-

8 and each human among 500 right-handed subjects randomly selected from the HCP-YA dataset[105] with minimal preprocessing[106]. Each vertex of the white/gray matter surface was seeded for probabilistic tractography with the whole brain as the target to generate a vertex-wise connectivity matrix. Then, it was multiplied by the vectorized tract map that described the trajectory of each tract in the brain and was normalized to get the connectivity profiles of each vertex with the 42 tracts. Finally, we averaged the connectivity profiles of the vertices within each region of the MacBNA and HumBNA to form the regional connectivity blueprints across subjects. In other words, the connectivity blueprints represent the connection of each cortical region to the 42 major white bundles. The parameters were set as a default of the XTRACT tool. The symmetric Kullback-Leibler (KL) divergence was used to measure the similarity of the group-wise connectivity blueprints between each region of MacBNA and each region of HumBNA. The divergence map represents the minimal KL divergence of each region in the human from the macaque regions. The divergence map was compared using the Spearman's correlation with another brain maps that are provided in neuromaps[49].

The regional gene expression of the HumBNA was estimated with the Allen Human Brain Atlas (AHBH) transcriptome dataset[50] using abagen[107], resulting in 15633 remaining genes. Only the left hemisphere was considered since the AHBH has probe samples in the right hemisphere for only two subjects[108]. A partial least squares regression (PLSR) between the divergence map and gene expression was performed to characterize the genetic mechanism underlying the structural variation between the two species. To avoid overfitting, only the genes that significantly correlated with the divergence map ($P < .05$) were retained for the subsequent PLSR analysis. PLSR has been widely used to bridge the relationship between neuroimaging and the transcriptome because it determines the most predictive genes with a weighted score of the neuroimaging map[109–111]. 10000 surrogate maps, which were generated by Brainsmash[112], were used to ensure that the explained variance of the first PLSR component (PLS1 score) was significantly higher than that generated by chance. The correlation between the divergence map and the PLS1 score was examined as described above. Then, 1000 bootstrapping was used to estimate the error of the weight of each gene, and the normalized weight (Z) of each gene was denoted as the weight divided by the estimated error[111]. We quantified the enrichment of the statistically significant genes ($|Z| > 3$, 2253 genes remained) in the disease-related gene sets, which we obtained from DisGeNet[113], with all the human genes as the background using Metascape[114] software. Finally, we tested

whether these significant genes overlapped more with human-accelerated genes (HAR genes)[52] using Fisher's exact test.

Statistical Significance using Permutated Brain Data

Due to the spatial autocorrelation of the brain data, we tested the statistical significance (P_{spin}) of the findings by generating surrogate brain maps that preserved the spatial autocorrelation using BrainSMASH[112]. The number of permutation samples was 10000, if not specifically stated.

Data and Code Availability

The ex vivo MRI data of the Brainnetom-8, the MRI images and sections of another postmortem monkey, and the code of the parcellation pipeline based on the surface will be openly available at https://molicaca.github.io/atlas/mcqatlas.html upon acceptance.

Competing Interests Statement

The authors declare that they have no conflict of interest.

Acknowledgements

This work was partially supported by the Science and Technology Innovation 2030 - Brain Science and Brain-Inspired Intelligence Project (Grant No. 2021ZD0200200), Natural Science Foundation of China (Grant Nos. 82151307, 82202253, and 31620103905), Strategic Priority Research Program of the Chinese Academy of Sciences (XDB32030207), and Science Frontier Program of the Chinese Academy of Sciences (grant No. QYZDJ-SSW-SMC019).

References

1. Van Essen, D. C. *et al.* Cerebral cortical folding, parcellation, and connectivity in humans, nonhuman primates, and mice. *Proc. Natl. Acad. Sci.* **116**, 26173–26180 (2019).
2. Gray, D. T. & Barnes, C. A. Experiments in macaque monkeys provide critical insights into age-associated changes in cognitive and sensory function. *Proc. Natl. Acad. Sci.* **116**, 26247–26254 (2019).
3. Milham, M. P. *et al.* An Open Resource for Non-human Primate Imaging. *Neuron* **100**, 61-74.e2 (2018).
4. Autio, J. A. *et al.* Minimal specifications for non-human primate MRI: Challenges in standardizing and harmonizing data collection. *NeuroImage* **236**, 118082 (2021).
5. Hayashi, T. *et al.* The nonhuman primate neuroimaging and neuroanatomy project. *NeuroImage* **229**, 117726 (2021).
6. Van Essen, D. C. & Glasser, M. F. Parcellating Cerebral Cortex: How Invasive Animal Studies Inform Noninvasive Mapmaking in Humans. *Neuron* **99**, 640–663 (2018).
7. Eickhoff, S. B., Yeo, B. T. T. & Genon, S. Imaging-based parcellations of the human brain. *Nat. Rev. Neurosci.* **19**, 672–686 (2018).
8. Van Essen, D. C., Donahue, C., Dierker, D. L. & Glasser, M. F. Parcellations and Connectivity Patterns in Human and Macaque Cerebral Cortex. in *Micro-, Meso- and Macro-Connectomics of the Brain* (eds. Kennedy, H., Van Essen, D. C. & Christen, Y.) (Springer, 2016).
9. Caspers, S., Eickhoff, S. B., Zilles, K. & Amunts, K. Microstructural grey matter parcellation and its relevance for connectome analyses. *NeuroImage* **80**, 18–26 (2013).

10. Amunts, K. *et al.* BigBrain: An Ultrahigh-Resolution 3D Human Brain Model. *Science* **340**, 1472–1475 (2013).

11. Alkemade, A. *et al.* A unified 3D map of microscopic architecture and MRI of the human brain. *Sci. Adv.* **8**, eabj7892 (2022).

12. Brodmann, K. Beitraege zur histologischen lokalisation der grosshirnrinde. IIIte mitteilung: Die rindenfelder der niederen affen. *J. Fuer Psychol. Neurol.* **4**, 177–226 (1905).

13. Walker, A. E. A cytoarchitectural study of the prefrontal area of the macaque monkey. *J. Comp. Neurol.* **73**, 59–86 (1940).

14. Lewis, J. W. & Van Essen, D. C. Mapping of architectonic subdivisions in the macaque monkey, with emphasis on parieto-occipital cortex. *J. Comp. Neurol.* **428**, 79–111 (2000).

15. Hartig, R. *et al.* The Subcortical Atlas of the Rhesus Macaque (SARM) for neuroimaging. *NeuroImage* **235**, 117996 (2021).

16. Saleem, K. S. & Logothetis, N. K. *A combined MRI and histology atlas of the rhesus monkey brain in stereotaxic coordinates*. (Amsterdam, The Netherlands, 2007).

17. Preuss, T. M. & Goldman-Rakic, P. S. Myelo- and cytoarchitecture of the granular frontal cortex and surrounding regions in the strepsirhine primate Galago and the anthropoid primate Macaca. *J. Comp. Neurol.* **310**, 429–474 (1991).

18. Paxinos, G. *The rhesus monkey brain in stereotaxic coordinates*. (Academic, 2009).

19. Jung, B. *et al.* A comprehensive macaque fMRI pipeline and hierarchical atlas. *NeuroImage* **235**, 117997 (2021).

679 20. Johansen-Berg, H. *et al.* Changes in connectivity profiles define functionally distinct regions in human
680 medial frontal cortex. *Proc. Natl. Acad. Sci.* **101**, 13335–13340 (2004).
681 21. Beckmann, M., Johansen-Berg, H. & Rushworth, M. F. S. Connectivity-based parcellation of human
682 cingulate cortex and its relation to functional specialization. *J. Neurosci. Off. J. Soc. Neurosci.* **29**, 1175–
683 1190 (2009).
684 22. Saygin, Z. M. *et al.* Anatomical connectivity patterns predict face selectivity in the fusiform gyrus. *Nat.*
685 *Neurosci.* **15**, 321–327 (2012).
686 23. Osher, D. E. *et al.* Structural Connectivity Fingerprints Predict Cortical Selectivity for Multiple Visual
687 Categories across Cortex. *Cereb. Cortex* **26**, 1668–1683 (2016).
688 24. Wu, D. *et al.* Hierarchy of Connectivity–Function Relationship of the Human Cortex Revealed through
689 Predicting Activity across Functional Domains. *Cereb. Cortex* **30**, 4607–4616 (2020).
690 25. Passingham, R. E., Stephan, K. E. & Kötter, R. The anatomical basis of functional localization in the
691 cortex. *Nat. Rev. Neurosci.* **3**, 606–616 (2002).
692 26. Fan, L. *et al.* The Human Brainnetome Atlas: A New Brain Atlas Based on Connectional Architecture.
693 *Cereb. Cortex* **26**, 3508–3526 (2016).
694 27. Liu, C. *et al.* A digital 3D atlas of the marmoset brain based on multi-modal MRI. *NeuroImage* **169**, 106–
695 116 (2018).
696 28. Cerliani, L., D'Arceuil, H. & Thiebaut de Schotten, M. Connectivity-based parcellation of the macaque
697 frontal cortex, and its relation with the cytoarchitectonic distribution described in current atlases. *Brain*
698 *Struct. Funct.* **222**, 1331–1349 (2017).

29. Cheng, L. *et al.* Connectional asymmetry of the inferior parietal lobule shapes hemispheric specialization in humans, chimpanzees, and rhesus macaques. *eLife* **10**, e67600 (2021).

30. Xia, X. *et al.* Fine-Grained Parcellation of the Macaque Nucleus Accumbens by High-Resolution Diffusion Tensor Tractography. *Front. Neurosci.* **13**, (2019).

31. He, B. *et al.* Fine-Grained Topography and Modularity of the Macaque Frontal Pole Cortex Revealed by Anatomical Connectivity Profiles. *Neurosci. Bull.* **36**, 1454–1473 (2020).

32. Schotten, M. T. de, Urbanski, M., Valabregue, R., Bayle, D. J. & Volle, E. Subdivision of the occipital lobes: An anatomical and functional MRI connectivity study. *Cortex* **56**, 121–137 (2014).

33. Ambrosen, K. S. *et al.* Validation of structural brain connectivity networks: The impact of scanning parameters. *NeuroImage* **204**, (2020).

34. Donahue, C. J. *et al.* Using diffusion tractography to predict cortical connection strength and distance: A quantitative comparison with tracers in the monkey. *J. Neurosci.* **36**, 6758–6770 (2016).

35. Liu, C. *et al.* Marmoset Brain Mapping V3: Population multi-modal standard volumetric and surface-based templates. *NeuroImage* **226**, 117620 (2021).

36. Li, K. *et al.* The human mediodorsal thalamus: Organization, connectivity, and function. *NeuroImage* **249**, 118876 (2022).

37. Schurr, R. & Mezer, A. A. The glial framework reveals white matter fiber architecture in human and primate brains. *Science* **374**, 762–767 (2021).

38. Folloni, D. *et al.* Dichotomous organization of amygdala/temporal-prefrontal bundles in both humans and monkeys. *eLife* **8**, (2019).

39. Shen, K. *et al.* A macaque connectome for large-scale network simulations in TheVirtualBrain. *Sci. Data* **6**, 123 (2019).

40. Noonan, M. P. *et al.* A Neural Circuit Covarying with Social Hierarchy in Macaques. *PLOS Biol.* **12**, e1001940 (2014).

41. Weiss, A. R. *et al.* The macaque brain ONPRC18 template with combined gray and white matter labelmap for multimodal neuroimaging studies of Nonhuman Primates. *NeuroImage* **225**, 117517 (2021).

42. Nakajima, R., Kinoshita, M., Shinohara, H. & Nakada, M. The superior longitudinal fascicle: reconsidering the fronto-parietal neural network based on anatomy and function. *Brain Imaging Behav.* **14**, 2817–2830 (2020).

43. Markov, N. T. *et al.* A Weighted and Directed Interareal Connectivity Matrix for Macaque Cerebral Cortex. *Cereb. Cortex* **24**, 17–36 (2012).

44. Saleem, K. S. *et al.* High-resolution mapping and digital atlas of subcortical regions in the macaque monkey based on matched MAP-MRI and histology. *NeuroImage* **245**, 118759 (2021).

45. Fischl, B. FreeSurfer. *NeuroImage* **62**, 774–781 (2012).

46. Xu, T. *et al.* Cross-species functional alignment reveals evolutionary hierarchy within the connectome. *NeuroImage* **223**, 117346 (2020).

47. van der Maaten, L.J.P. & Hinton, G.E. Visualizing High-Dimensional Data Using t-SNE. *J. Mach. Learn. Res.* **9**, 2579–2605 (2008).

48. Mars, R. B. *et al.* Whole brain comparative anatomy using connectivity blueprints. *eLife* **7**, (2018).

49. Markello, R. D. *et al.* neuromaps: structural and functional interpretation of brain maps. *Nat. Methods* 1–8 (2022) doi:10.1038/s41592-022-01625-w.

740 50. Hawrylycz, M. J. *et al.* An anatomically comprehensive atlas of the adult human brain transcriptome.
741 *Nature* **489**, 391–399 (2012).
742 51. Piñero, J. *et al.* The DisGeNET knowledge platform for disease genomics: 2019 update. *Nucleic Acids*
743 *Res.* **48**, D845–D855 (2020).
744 52. Wei, Y. *et al.* Genetic mapping and evolutionary analysis of human-expanded cognitive networks. *Nat.*
745 *Commun.* **10**, 4839 (2019).
746 53. Rakic, P., Suñer, I. & Williams, R. W. A novel cytoarchitectonic area induced experimentally within the
747 primate visual cortex. *Proc. Natl. Acad. Sci.* **88**, 2083–2087 (1991).
748 54. Pallas, S. L. Intrinsic and extrinsic factors that shape neocortical specification. *Trends Neurosci.* **24**, 417–
749 423 (2001).
750 55. Niu, M. *et al.* Organization of the Macaque Monkey Inferior Parietal Lobule Based on Multimodal
751 Receptor Architectonics. *NeuroImage* 117843 (2021).
752 56. Pandya, D. N. & Seltzer, B. Intrinsic connections and architectonics of posterior parietal cortex in the
753 rhesus monkey. *J. Comp. Neurol.* **204**, 196–210 (1982).
754 57. Delhaye, B. P., Long, K. H. & Bensmaia, S. J. Neural Basis of Touch and Proprioception in Primate Cortex.
755 in *Comprehensive Physiology* 1575–1602 (John Wiley & Sons, Ltd, 2018).
756 58. Kaas, J. H. Evolution of columns, modules, and domains in the neocortex of primates. *Proc. Natl. Acad.*
757 *Sci.* **109**, 10655–10660 (2012).
758 59. Young, N. A., Collins, C. E. & Kaas, J. H. Cell and neuron densities in the primary motor cortex of
759 primates. *Front. Neural Circuits* **7**, (2013).

60. Knösche, T. & Tittgemeyer, M. The Role of Long-Range Connectivity for the Characterization of the Functional–Anatomical Organization of the Cortex. *Front. Syst. Neurosci.* **5**, (2011).

61. van den Heuvel, M. P. & Yeo, B. T. T. A Spotlight on Bridging Microscale and Macroscale Human Brain Architecture. *Neuron* **93**, 1248–1251 (2017).

62. Cloutman, L. & Lambon Ralph, M. Connectivity-based structural and functional parcellation of the human cortex using diffusion imaging and tractography. *Front. Neuroanat.* **6**, (2012).

63. Rozzi, S., Ferrari, P. F., Bonini, L., Rizzolatti, G. & Fogassi, L. Functional organization of inferior parietal lobule convexity in the macaque monkey: electrophysiological characterization of motor, sensory and mirror responses and their correlation with cytoarchitectonic areas. *Eur. J. Neurosci.* **28**, 1569–1588 (2008).

64. Germann, J. & Petrides, M. Area 8A within the Posterior Middle Frontal Gyrus Underlies Cognitive Selection between Competing Visual Targets. *eNeuro* **7**, (2020).

65. Rapan, L. *et al.* Multimodal 3D atlas of the macaque monkey motor and premotor cortex. *NeuroImage* **226**, 117574 (2021).

66. Dong, H.-M., Margulies, D. S., Zuo, X.-N. & Holmes, A. J. Shifting gradients of macroscale cortical organization mark the transition from childhood to adolescence. *Proc. Natl. Acad. Sci.* **118**, (2021).

67. Vos de Wael, R. *et al.* BrainSpace: a toolbox for the analysis of macroscale gradients in neuroimaging and connectomics datasets. *Commun. Biol.* **3**, 103 (2020).

68. Blazquez Freches, G. *et al.* Principles of temporal association cortex organisation as revealed by connectivity gradients. *Brain Struct. Funct.* **225**, 1245–1260 (2020).

69. Genon, S. *et al.* The heterogeneity of the left dorsal premotor cortex evidenced by multimodal connectivity-based parcellation and functional characterization. *NeuroImage* **170**, 400–411 (2018).

70. Kringelbach, M. L. & Rolls, E. T. The functional neuroanatomy of the human orbitofrontal cortex: evidence from neuroimaging and neuropsychology. *Prog. Neurobiol.* **72**, 341–372 (2004).

71. Mars, R. B., Jbabdi, S. & Rushworth, M. F. S. A Common Space Approach to Comparative Neuroscience. *Annu. Rev. Neurosci.* **44**, 69–86 (2021).

72. Bor, D. & Seth, A. Consciousness and the Prefrontal Parietal Network: Insights from Attention, Working Memory, and Chunking. *Front. Psychol.* **3**, (2012).

73. Barbey, A. K. *et al.* An integrative architecture for general intelligence and executive function revealed by lesion mapping. *Brain* **135**, 1154–1164 (2012).

74. Vaishnavi, S. N. *et al.* Regional aerobic glycolysis in the human brain. *Proc. Natl. Acad. Sci.* **107**, 17757–17762 (2010).

75. Crow, T. J. Is schizophrenia the price that Homo sapiens pays for language? *Schizophr. Res.* **28**, 127–141 (1997).

76. van den Heuvel, M. P. *et al.* Evolutionary modifications in human brain connectivity associated with schizophrenia. *Brain* **142**, 3991–4002 (2019).

77. Nichols, C. Is there an evolutionary advantage of schizophrenia? *Personal. Individ. Differ.* **46**, 832–838 (2009).

78. Reardon, S. Geneticists are starting to unravel evolution's role in mental illness. *Nature* **551**, 15–16 (2017).

79. Tendler, B. C. *et al.* The Digital Brain Bank, an open access platform for post-mortem imaging datasets. *eLife* **11**, e73153 (2022).

80. Yendiki, A. *et al.* Post mortem mapping of connectional anatomy for the validation of diffusion MRI. *NeuroImage* **256**, 119146 (2022).

81. Sotiropoulos, S. N. *et al.* Advances in diffusion MRI acquisition and processing in the Human Connectome Project. *NeuroImage* **80**, 125–143 (2013).

82. Heidemann, R. M., Anwander, A., Feiweier, T., Knösche, T. R. & Turner, R. k-space and q-space: Combining ultra-high spatial and angular resolution in diffusion imaging using ZOOPPA at 7T. *NeuroImage* **60**, 967–978 (2012).

83. Liu, C. *et al.* A resource for the detailed 3D mapping of white matter pathways in the marmoset brain. *Nat. Neurosci.* **23**, 271–280 (2020).

84. Jbabdi, S., Sotiropoulos, S. N., Savio, A. M., Graña, M. & Behrens, T. E. J. Model-based analysis of multishell diffusion MR data for tractography: How to get over fitting problems. *Magn. Reson. Med.* **68**, 1846–1855 (2012).

85. Setsompop, K. *et al.* Pushing the limits of in vivo diffusion MRI for the Human Connectome Project. *NeuroImage* **80**, 220–233 (2013).

86. Reveley, C. *et al.* Diffusion MRI anisotropy in the cerebral cortex is determined by unmyelinated tissue features. *Nat. Commun.* **13**, 6702 (2022).

87. Autio, J. A. *et al.* Towards HCP-Style Macaque Connectomes: 24-Channel 3T Multi-Array Coil, MRI Sequences and Preprocessing. *NeuroImage* 116800 (2020).

88. Calabrese, E. *et al.* A diffusion tensor MRI atlas of the postmortem rhesus macaque brain. *NeuroImage* **117**, 408–416 (2015).

821 89. Woolrich, M. W. *et al.* Bayesian analysis of neuroimaging data in FSL. *NeuroImage* **45**, S173–S186
822 (2009).
823 90. Tournier, J.-D. *et al.* MRtrix3: A fast, flexible and open software framework for medical image processing
824 and visualisation. *NeuroImage* **202**, 116137 (2019).
825 91. Tustison, N. J. *et al.* N4ITK: Improved N3 bias correction. *IEEE Trans. Med. Imaging* **29**, 1310–1320
826 (2010).
827 92. Xu, T. *et al.* Delineating the Macroscale Areal Organization of the Macaque Cortex In Vivo. *Cell Rep.* **23**,
828 429–441 (2018).
829 93. Tian, X. *et al.* An integrated resource for functional and structural connectivity of the marmoset brain. *Nat.*
830 *Commun.* **13**, 7416 (2022).
831 94. Reveley, C. *et al.* Three-Dimensional Digital Template Atlas of the Macaque Brain. *Cereb. Cortex* **27**,
832 4463–4477 (2016).
833 95. Rushmore, R. J. *et al.* MRI-based Parcellation and Morphometry of the Individual Rhesus Monkey Brain:
834 the macaque Harvard-Oxford Atlas (mHOA), a translational system referencing a standardized ontology.
835 *Brain Imaging Behav.* (2020).
836 96. Li, H. *et al.* ATPP: A Pipeline for Automatic Tractography-Based Brain Parcellation. *Front.*
837 *Neuroinformatics* **11**, (2017).
838 97. Zhu, Y., Tian, D. & Yan, F. Effectiveness of Entropy Weight Method in Decision-Making. *Math. Probl.*
839 *Eng.* **2020**, e3564835 (2020).
840 98. Seidlitz, J. *et al.* A population MRI brain template and analysis tools for the macaque. *NeuroImage* **170**,
841 121–131 (2018).

842 99. Avants, B. B., Tustison, N. J., Wu, J., Cook, P. A. & Gee, J. C. An Open Source Multivariate Framework
843 for n-Tissue Segmentation with Evaluation on Public Data. *Neuroinformatics* **9**, 381–400 (2011).
844 100. Markov, N. T. *et al.* The role of long-range connections on the specificity of the macaque interareal cortical
845 network. *Proc. Natl. Acad. Sci.* **110**, 5187–5192 (2013).
846 101. Zhi, D., King, M., Hernandez-Castillo, C. R. & Diedrichsen, J. Evaluating brain parcellations using the
847 distance-controlled boundary coefficient. *Hum. Brain Mapp.* **43**, 3706–3720 (2022).
848 102. Hao, Y. *et al.* EdgeFlow: Achieving Practical Interactive Segmentation with Edge-Guided Flow.
849 *ArXiv210909406 Cs* (2021).
850 103. Mori, S., Crain, B. J., Chacko, V. P. & van Zijl, P. C. Three-dimensional tracking of axonal projections in
851 the brain by magnetic resonance imaging. *Ann. Neurol.* **45**, 265–269 (1999).
852 104. Warrington, S. *et al.* XTRACT - Standardised protocols for automated tractography in the human and
853 macaque brain. *NeuroImage* 116923 (2020).
854 105. Van Essen, D. C. *et al.* The Human Connectome Project: a data acquisition perspective. *NeuroImage* **62**,
855 2222–2231 (2012).
856 106. Glasser, M. F. *et al.* The minimal preprocessing pipelines for the Human Connectome Project.
857 *NeuroImage* **80**, 105–124 (2013).
858 107. Markello, R., Shafiei, G., Zheng, Y.-Q. & Mišić, B. abagen: A toolbox for the Allen Brain Atlas genetics
859 data. (2020) doi:10.5281/zenodo.3688800.
860 108. Arnatkeviciute, A., Fulcher, B. D. & Fornito, A. A practical guide to linking brain-wide gene expression
861 and neuroimaging data. *NeuroImage* **189**, 353–367 (2019).
862 109. Chen, P. *et al.* Altered global signal topography in Alzheimer's disease. *eBioMedicine* **89**, (2023).

110. Shi, W. *et al.* Two subtypes of schizophrenia identified by an individual-level atypical pattern of tensor-based morphometric measurement. *Cereb. Cortex* bhac301 (2022).

111. Morgan, S. E. *et al.* Cortical patterning of abnormal morphometric similarity in psychosis is associated with brain expression of schizophrenia-related genes. *Proc. Natl. Acad. Sci.* **116**, 9604–9609 (2019).

112. Burt, J. B., Helmer, M., Shinn, M., Anticevic, A. & Murray, J. D. Generative modeling of brain maps with spatial autocorrelation. *NeuroImage* **220**, 117038 (2020).

113. Piñero, J. *et al.* DisGeNET: a comprehensive platform integrating information on human disease-associated genes and variants. *Nucleic Acids Res.* **45**, D833–D839 (2017).

114. Zhou, Y. *et al.* Metascape provides a biologist-oriented resource for the analysis of systems-level datasets. *Nat. Commun.* **10**, 1523 (2019).

Figures

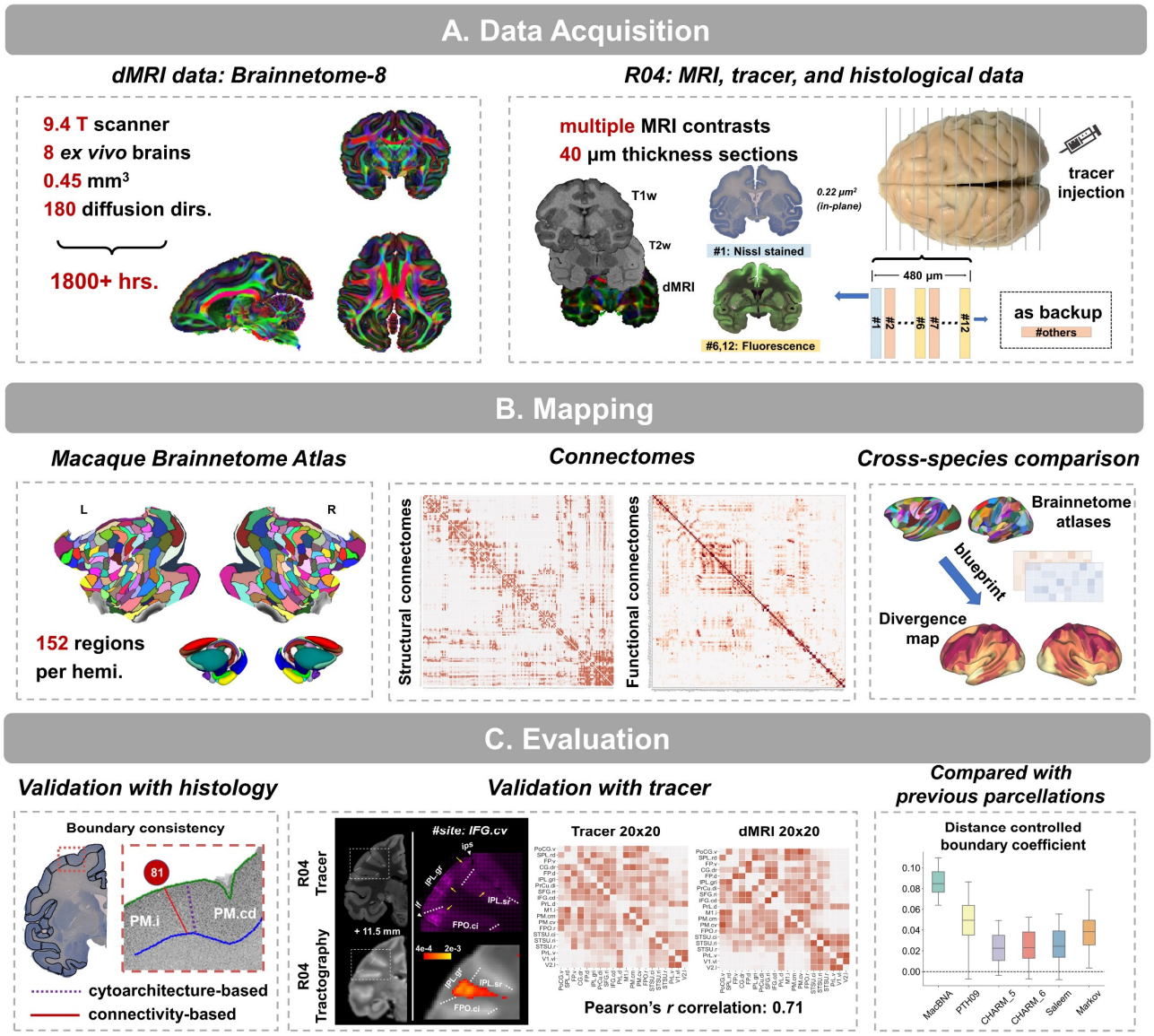

Fig. 1 | Overview of the data, mapping, and evaluation of the Macaque Brainnetome Atlas. (A) The high quality dMRI dataset Brainnetome-8 with eight ex vivo macaque brains and additional collected multi-modal and multi-scale data, including T1w, T2w, and diffusion MRI, Nissl-stained, and fluorescent tracer images for macaque R04. **(B)** A fine-grained structural connectivity-based atlas for macaques, i.e., Macaque Brainnetome Atlas (MacBNA) was delineated using high-quality Brainnetome-8 data, and regional structural and functional connectivity profiles were determined. An evolutional divergence map was constructed with structural connectivity blueprints based on the macaque and human Brainnetome atlases. **(C)** The Macaque Brainnetome Atlas was compared with cytoarchitectonic boundaries using the Nissl sections from R04. The structural connections were evaluated using the tracer images from R04 and an open-access tracer dataset.

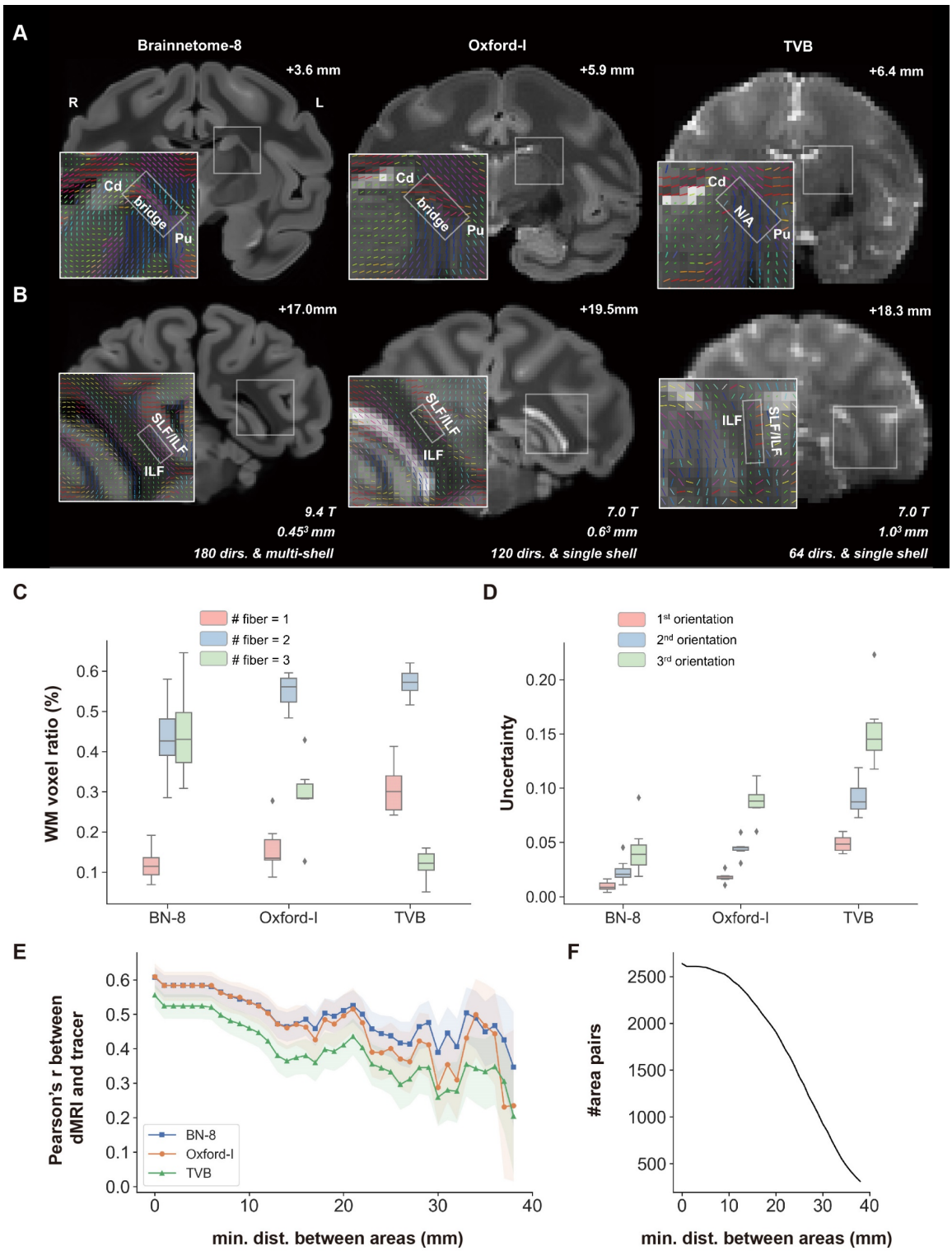

Fig. 2 | White matter structural comparisons of the Brainnetome-8, Oxford-I, and TVB dMRI datasets. (A-B) Visual inspection of the three datasets shows a substantial improvement of the Brainnetom-8 over the other datasets in that it captured the brain structures better. This can be attributed to its high spatial and angular resolution compared with the Oxford-I and TVB datasets. The structure highlighted in the white box is zoomed in at the left bottom corner of each coronal slice. **(C)** The ratio of white matter voxels that contain 1/2/3 fibers and **(D)** the uncertainty of each estimated fiber orientation provided by Bedpostx, indicating that more crossing fibers could be resolved and a sharper distribution of fiber orientations was estimated with

Brainnetome-8 **(E)** A higher correlation was found between the connections with Brainnetome-8 dMRI and tracer, taking the minimal distance between regions into consideration. Solid lines and shadings denote mean and standard deviation of the bootstrapped distributions, respectively. **(F)** The number of all paired regions at varying minimum interareal distance is shown. Abbreviations: *BN-8, Brainnetome-8; Cd, caudate nucleus; Pu, putamen; SLF, superior longitudinal fasciculus; ILF, inferior longitudinal fasciculus.*

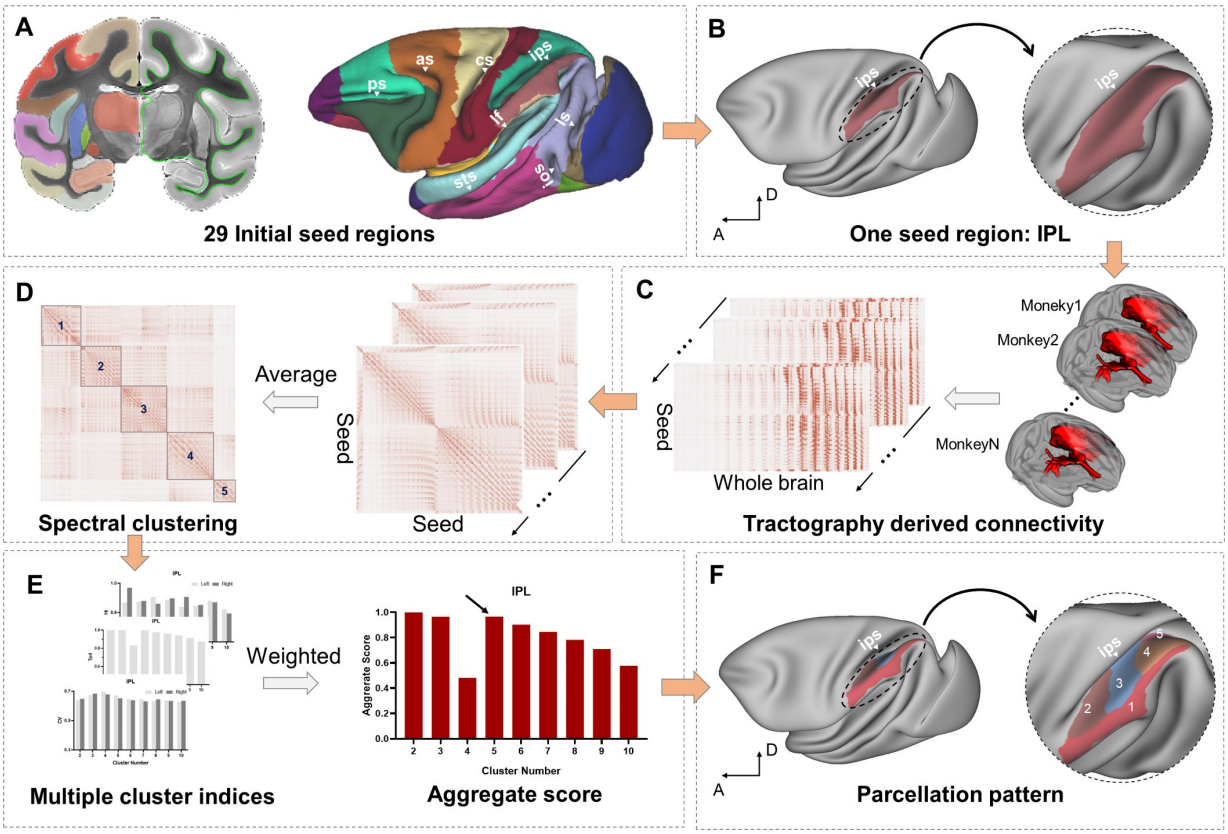

Fig. 3 Pipeline for the construction of the Macaque Brainnetome Atlas. (A) 29 initial seed regions of interest (ROIs), including 21 cortical and 8 subcortical regions, were manually delineated in volume space. The coronal view of the template brain shows the location of the anatomical seed regions as colored areas (left hemisphere) and as green lines on the white/gray surface (right hemisphere). Those seed regions were then mapped to the surface space to get surface-based ROIs for the cortical parcellation. (**B-F)** Surface-based parcellation of an exemplar seed region, IPL. **(C)** Probabilistic tractography was performed from each vertex seed to the whole brain and the connectivity profile was stored in a connectivity matrix (seed-by-whole brain) for each subject. **(D)** Pairwise correlations of voxels in the seed region were calculated to get a similarity matrix (seed-by-seed) for each subject, and spectral clustering was conducted on the averaged similarity matrix across all subjects. **(E)** Three indices, CV, Tpd, and Hi, were fused to form an aggregate score based on entropy theory to estimate the optimal cluster number (5 was the optimal cluster number as indicated by the location of the local maximum). **(F)** The parcellation pattern of the IPL. Abbreviations: *as, arcuate sulcus; cs, central sulcus; ps, principal sulcus; lf, lateral fissure; sts, superior temporal sulcus; ls, lunate sulcus; cgs, cingulate sulcus; ots, occipitotemporal sulcus; pos, parieto-occipital sulcus; iocs*, *inferior occipital sulcus*; *IPL, inferior parietal lobule.*

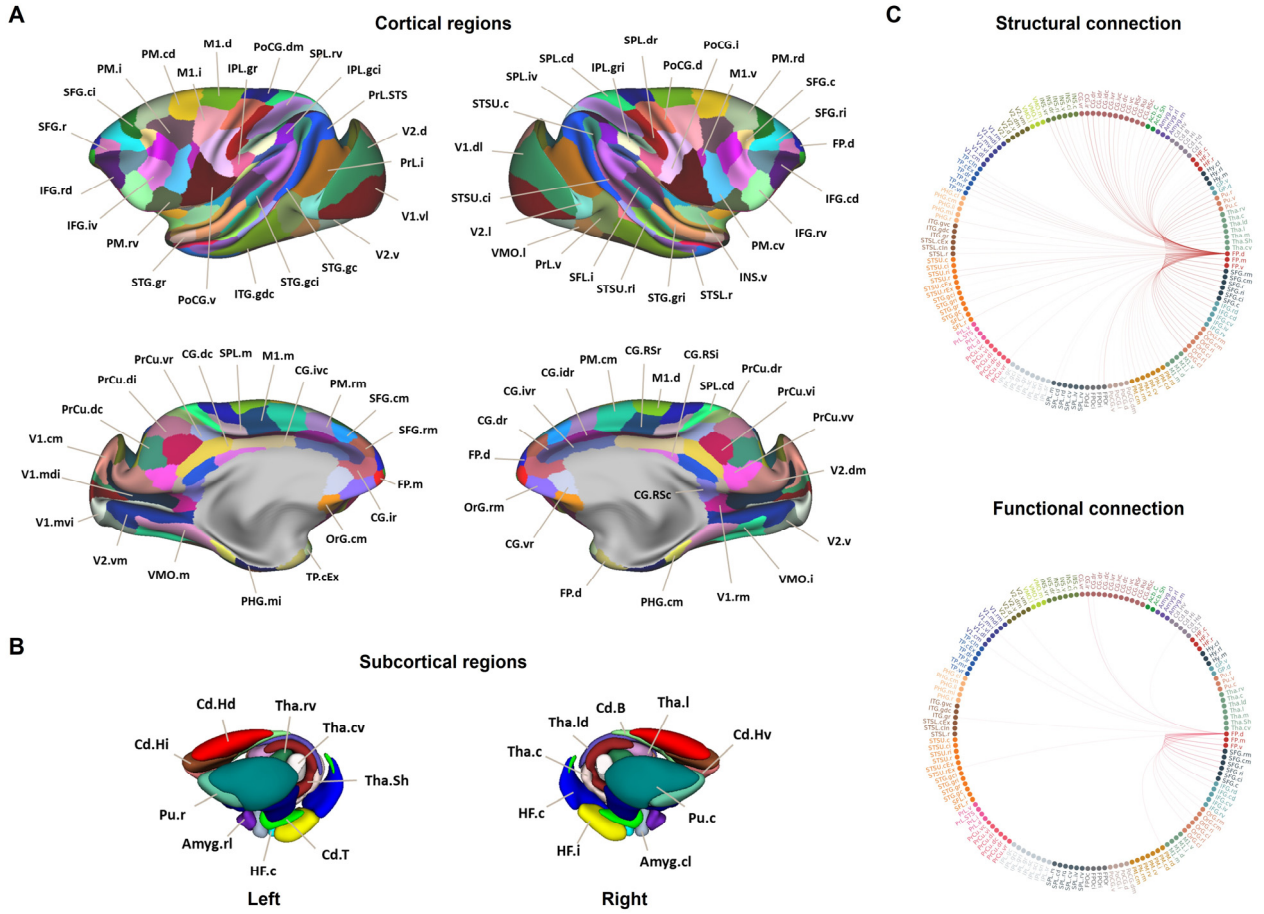

Fig. 4 | Overview of the Macaque Brainnetome Atlas. (A) Surface view of 248 cortical regions and **(B)** 3D view of 56 subcortical regions. **(C)** The left intra-hemisphere structural and resting-state functional connection of an exemplar region, FP.d. The nomenclature information for each subregion is listed in the Supplemental Nomenclature. Abbreviation: *FP.d, frontal pole dorsal part.*

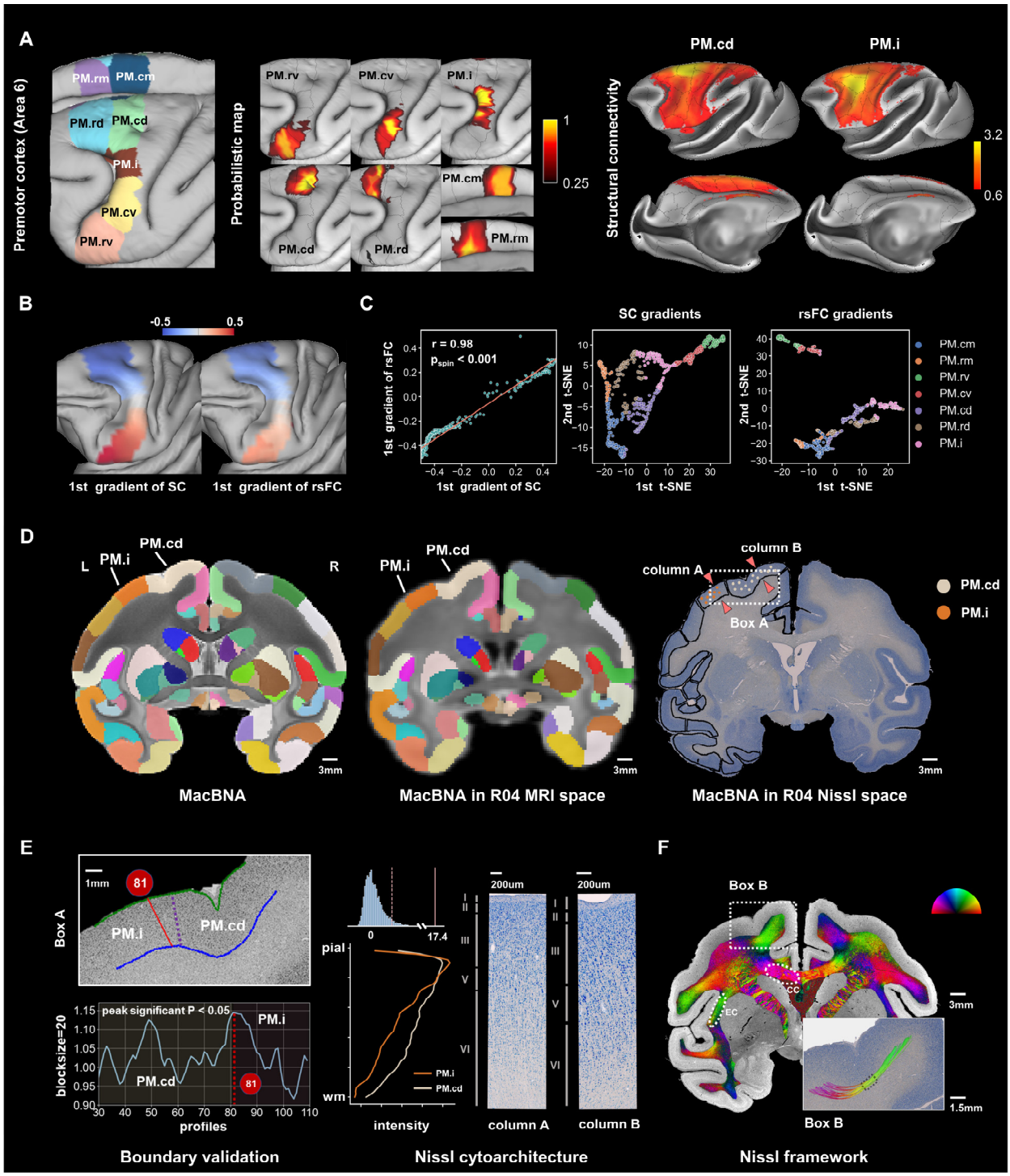

Fig. 5 | Macaque Brainnetome Atlas of the premotor cortex (PM) and the exemplar joint study with the MRI and Nissl images. (A) Left panel shows the parcellation of the PM in the MacBNA, which subdivided it into 7 regions. Middle panel is the population probabilistic map of each subregion of the PM, indicating the individual variation. Right panel is the structural connectivity of the PM.cd and PM.i with the whole brain. **(B)** The first gradient of the structural and resting-state functional connectivity of the PM. **(C)** The correlation between the two gradients and the visualization of the 7 clusters of the PM with the t-SNE. **(D)** Parcellations of the MacBNA in template, R04 MRI, and R04 Nissl space. The gray and orange dots mark the regions of the PM.cd and PM.i, respectively. **(E)** The zoom-in details (marked with white box) indicate the boundary between

the PM.cd and PM.i of the MacBNA (purple line) based on connectivity and the boundary (red line) determined using a quantitative cytoarchitecture analysis (left bottom). The middle panel is the mean density profile of the PM.cd and PM.i regions, and a permutation test with 10000 samples indicates the significant difference between their profiles ($P < .001$). The right panel shows the detailed laminar structures of two selected columns of the two regions that were marked in (D). **(F)** The fiber orientation reconstructed with the glial framework at a mesoscale spatial resolution (44 microns), and the white circles indicate two major tracts, i.e., CC and EC. The right bottom shows a tiny U-fiber connecting the neighboring gyral regions when seeding from the region below the sulci (black dotted box). Abbreviations: *PM, premotor cortex; PM.rd, premotor cortex rostrodorsal part; PM.cd, premotor cortex caudodorsal part; PM.i, premotor cortex intermediate part; PM.cv, premotor cortex caudoventral part; PM.rv, premotor cortex rostroventral part; PM.rm, premotor cortex rostromedial part; PM.cm, premotor cortex caudomedial part. CC,* c*orpus callosum; EC, external capsules*.

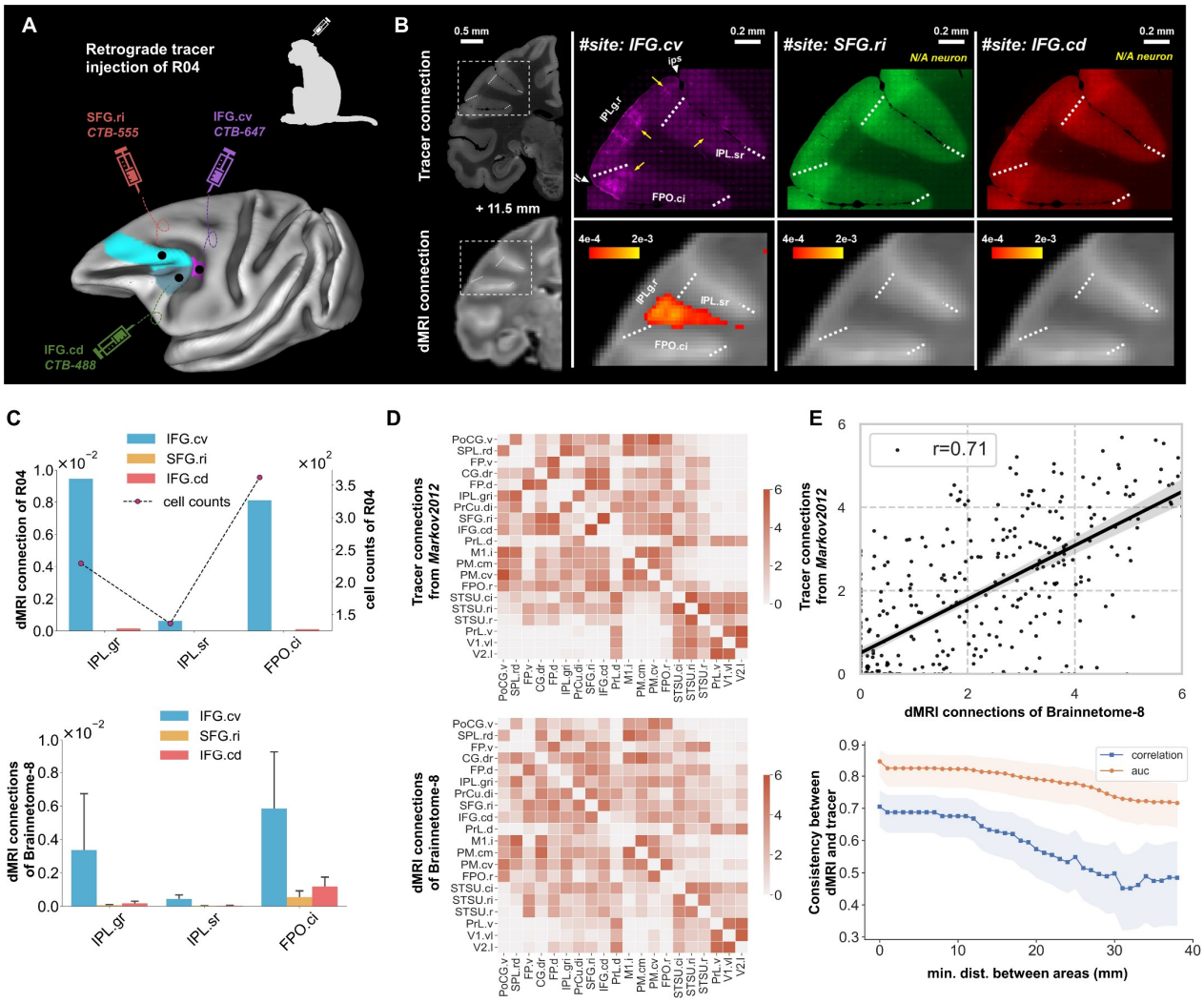

Fig. 6 | Evaluation of the MacBNA connections with tracers. (A) The R04 monkey was injected with retrograde tracers targeted at three regions of the MacBNA, the IFG.cv, SFG.ri, and IFG.cd, indicated with black circles**. (B)** The tracer connections with three projection regions IPL.gr, IPL.sr, and FPO.ci were qualitatively consistent with the tractography results from R04. The labeled neurons were marked with yellow arrows**.** Then, **(C)** the number of labeled neurons, which connected with IFG.cv, was quantitively compared with the normalized connections based on the dMRI results from R04 and Brainnetome-8. In addition, we compared the dMRI connections based on the MacBNA with the open-access tracer data taking the interareal distances into account. The 20x20 matrices of both the dMRI and tracer show **(D)** a similar pattern and **(E)** a high correlation (r = 0.71). Both matrices were also binarized to evaluate the sensitivity and specificity of the dMRI connections. Abbreviations: *IFG.cd, inferior frontal gyrus caudodorsal part; SFG.ri, superior frontal gyrus rostrointermediate part; IFG.cv, inferior frontal gyrus caudoventral part; IPL.gr, inferior parietal lobule gyral rostral part; IPL.sr, inferior parietal lobe, sulcal rostral part; FPO.ci, frontal parietal operculum caudointermediate part; auc, area-under-curve score.*

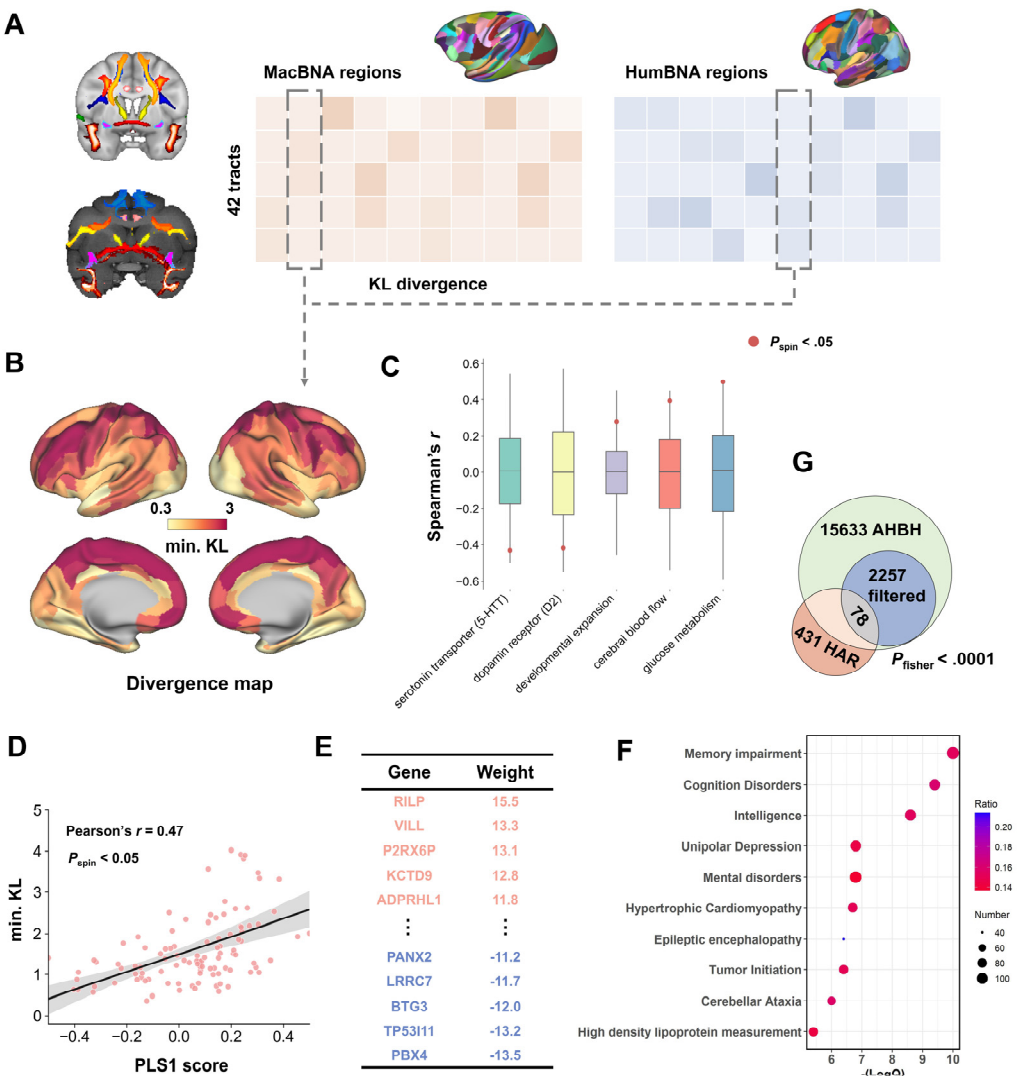

Fig. 7 | Structural divergence map between macaques and humans with the Brainnetome atlases and its association with transcriptome. (A) 42 homologous tracts of macaques and humans were identified to construct a common comparative space to measure the KL divergence between each pair of brain regions of macaques and humans using the blueprint connectivity. (B) The divergence map represents the minimal KL divergence of each region in humans from the macaque regions. (C) We compared the divergence map with other brain maps with neuromaps tool. The points represent the empirical Spearman's correlation between the divergence map and the other maps (red color indicate $P_{spin} < .05$). The boxplot represents the null distribution of the correlation between the 'rotated' divergence map with the other maps ($N = 10000$). (D) Correlation map of the divergence map with the PLS1 score of genes with the AHBH transcriptome dataset (left brain). (E) 2257 genes that have the most positive or negative weights ($|Z| > 3$) in PLSR were filtered for the subsequent gene ontology analysis. (F) The filtered 2257 genes were enriched in multiple gene sets that are associated with intelligence, cognition, and neuropsychiatric disorders. (G) 78 out of the 431 HAR genes (393 overlapped with 15633 AHBH genes) were included in the identified 2257 genes (Fisher's exact test $P < .0001$)